CHIRAL MULTI-ELECTRON EMISSION

Jamal BERAKDAR[a], Hubert KLAR[b]

[a]*Max-Planck-Institut für Mikrostrukturphysik, Weinberg 2, D-06120 Halle, Germany*
[b]*Theoretical Quantum Dynamics, Fakultät für Physik, Hermann-Herder-Straße 3, 79104 Freiburg, Germany*

ELSEVIER

AMSTERDAM – LONDON – NEW YORK – OXFORD – PARIS – SHANNON – TOKYO

ELSEVIER

Physics Reports 340 (2001) 473–520

PHYSICS REPORTS

www.elsevier.com/locate/physrep

Chiral multi-electron emission

Jamal Berakdar[a,*], Hubert Klar[b]

[a]*Max-Planck-Institut für Mikrostrukturphysik, Weinberg 2, D-06120 Halle, Germany*
[b]*Theoretical Quantum Dynamics, Fakultät für Physik, Hermann-Herder-Straße 3, 79104 Freiburg, Germany*

Received April 2000; editor: J. Eichler

Contents

1. Introduction 476
2. One-electron photoemission 477
3. Production of chiral electron pairs by one-photon absorption 479
   3.1. General analytical properties of the circular dichroism in one-photon two-electron transitions 479
   3.2. Propensity rules for the circular dichroism 483
   3.3. Alternative routes to the circular dichroism 485
   3.4. The circular dichroism and the role of the Pauli principle 487
   3.5. Consistency conditions 488
   3.6. Closed analytical expressions for the circular dichroism 490
   3.7. Dependence of the circular dichroism on the strength of the residual ion's field 492
   3.8. The photon-frequency dependence 492
   3.9. Calculational schemes of the polarised one-photon two-electron transitions 494
   3.10. The convergent close coupling technique 499
   3.11. Circular dichroism in the Auger-electron photoelectron spectroscopy 502
4. Chiral electron pair emission from laser-pumped atoms 503
   4.1. Formal development 504
   4.2. Symmetry relations of the orientational dichroism 507
   4.3. Analytical results 508
   4.4. Calculational schemes and experimental findings 509
5. Conclusions and outlook 513
Acknowledgements 515
Appendix A 515
   A.1. The analytical form of the circular dichroism 515
   A.2. Analytical expressions for the one-photon double-ionisation cross-section 517
References 517

* Corresponding author. Tel: + 49-345-5582666; fax: + 49-345-5511223.
E-mail address: jber@mpi-halle.de (J. Berakdar).

0370-1573/01/$ - see front matter
PII: S0370-1573(00)00083-1

Abstract

In this report we review recent progress in the understanding of the role of chirality in the multi-electron emission. A brief account of the chiral single-electron photoemission is given. In this case the chirality of the experimental set-up is brought about by an initial orientation of the target or/and by specifying a certain projection of the photoelectron spin. The dependence of the photoelectron spectrum on the chirality of the experiment is probed by changing the initial orientation of the target or by inverting the photoelectron spin projection. In a further section we envisage the direct transition of chiral electron pairs from an isotropic bound initial state into a double-continuum state following the absorption of a circularly polarised photon. We work out the necessary conditions under which the spectrum of the correlated photoelectron pair shows a chiral character, i.e. a dependence on the chirality of the exciting photon. The magnitude and the general behaviour of the chiral effects are estimated from simple analytical models and more elaborate numerical methods are presented for a more quantitative predictions. As a further example for the chiral multi-electron emission we study the photoelectron Auger-electron coincidence spectrum. The Auger hole is created by ionising a randomly oriented target by a circular polarised photon. We investigate how the helicity the photon is transferred to the emitted photoelectron pair. The theoretical findings are analysed and interpreted in light of recent experiments. In a final section we focus on the emission of correlated electrons where the initial state is already oriented, e.g. via optical pumping by circularly polarised light. The initial orientation of the atom is transferred to the continuum states following the ionisation of the target by low-energy electrons. We formulate and analyse the theoretical concepts for the transition of the screw sense of the initially bound atomic electron to the continuum electron pair. Numerical methods for the calculations of the cross-sections for the electron-impact ionisation of oriented atoms are presented and their results are contrasted against recent experimental data.

PACS: 33.55. − b; 32.80. − t

Keywords: Circular dichroism; Chirality; Photoionisation; One-photon double ionisation; Chirality in scattering reactions; Ionisation of oriented targets; Few particle scattering dynamics

1. Introduction

Since the early days of chemistry it has been observed that some compounds exist in two states that have similar physical and chemical properties. Their optical properties, however, are distinctively different: The plane of polarisation of the light passing through these chemicals is rotated in a different way. As it turned out the reason for this "optical activity" is a symmetry break caused by the special inner construction of the optically active molecules [1]. These compounds possess two different molecular structures that are mirror images of each other just like the left and the right hand. This special case of spatial symmetry has been termed "stereoisomery". Stereoisomery occurs only when the molecules are spatially asymmetric or "chiral", as termed by Lord Keliv, i.e. if they do not possess a symmetry plane.

The reduction of symmetry, regardless of the way this reduction has been brought about, is in fact the underlying reason for the optical activity. As demonstrated experimentally [2] the optical activity can indeed be increased by sculpturing thin films that reveals appropriate chirality. Another well established example of the symmetry reduction leading to optical effects is observed in magnetic materials. In this case the presence of a time reversal symmetry-breaking magnetisation of the medium results in a non-reciprocal optical effects, such as the polarisation rotation. For metallic, reflecting media, this phenomenon is known as the magneto-optical Kerr effect whereas for transparent media it is called the Faraday effect [3].

Chirality can also be introduced in the reaction via a suitable choice of the experimental set-up [4,5]. For example, in Ref. [6] two input laser beams (a control and a probe beam) have been used to study second harmonic generation from achiral thin films with in-plane isotropy, i.e. the sample as such has no chirality. The linear polarisation of the control beam breaks the reflection symmetry of the set-up leading thus to a different second harmonic efficiency for a left and a right-handed circular polarisation of the probe beam. A further example of an experiment-induced chirality is the photoelectron emission from oriented linear molecules. As a matter of definition, a chiral linear molecule does not exist, for an arbitrary plane containing the molecular bond can always be chosen as a plane of symmetry. However, for linear molecules either adsorbed on surfaces [7] or fixed in space [8] chirality can be triggered by angular-resolved photoemission experiments. In this case, the molecular axis, the direction of the incident radiation and the momentum vector of the photoelectron form a right-handed frame whose left-handed reflection is being well defined and experimentally controllable, e.g. by flipping the helicity of the impinging photon [9–14].

For atoms the situation is slightly different due to the absence of the molecular bond axis. In fact, single photoionisation of unpolarised atoms is insensitive to the helicity of the photon and thus the photoelectron spectra show no chiral effects [15,16]. Nonetheless, it is possible to observe chiral effects in atomic systems by constructing a chiral experimental set-up. This can be achieved, e.g., by performing the photoionisation experiment with the spin of the photoelectron being resolved [17–21]. In this case a co-ordinate system with well-defined orientation can be formed by the wave vector of the photon, the spin projection of the emitted photoelectron and the photoelectron's vector momentum. Alternatively, one might dismiss the laborious spin detection of the photoelectrons but use instead optical pumping to polarise the bound initial state [22–31]. A chiral effect appears then because the orientation of the target, the photon's wave vector and the vector momentum of the ionised electron build a right or a left handed co-ordinate frame depending, for example, on the orientation of the initial state. For naturally polarised targets, such as magnetised

samples, this dichroic effect serves as a standard method for the investigation of element selective magnetic properties [32–35].

In recent years, it became clear that chirality can also be observed in one photon two-electron emission from completely isotropic targets and without resolving the spins of the photoelectrons [36–54]. In this case, which is the subject of the present article, the co-ordinate frame is spanned by the vector momenta of the two photoelectrons ($\boldsymbol{k}_a$ and $\boldsymbol{k}_b$) and the wave vector of the photon $\boldsymbol{k}$. Since the photon is absorbed by the two photoelectrons and since the target initial state and the residual ion state are achiral, one can argue that the chirality of the photon is transferred to the two electron pair. That is, the pair attains a chirality as an internal degree of freedom that can be probed by varying the helicity of the photon. At first sight the occurrence of such a chirality may seem surprising as the initial target has no internal sense of rotation and the final state attains its chiral character by resolving the wave vectors of the two photoelectrons. On the other hand, due to the Pauli principle, the experimental out-come has to be invariant under the exchange of the two photoelectrons. However, as illustrated in Section 3, the orientation of the co-ordinate system (spanned by $\boldsymbol{k}_a$, $\boldsymbol{k}_b$ and $\boldsymbol{k}$) is inverted only when $\hat{\boldsymbol{k}}_a$ and $\hat{\boldsymbol{k}}_b$ or k_a and k_b are inverted but not when $\boldsymbol{k}_a$ is replaced by $\boldsymbol{k}_b$. This subtle feature of "chiral two-electron" photoionisation is unravelled by a formal mathematical analysis presented in Section 3 which gives insight into the geometrical structure of the chiral effect. Furthermore, we discuss in Section 3 the interplay between geometry and dynamics and point out ways and models to quantify and present the phenomena of chirality in two-electron photoemission.

As mentioned above, the orientation of an atomic target, e.g. via optical pumping, results in photoelectron spectra that are sensitive to the helicity of the photon. This dichroic effect has also been observed in the scattering of charged particle from oriented targets, in particular in the capture channel [55–57]. In this case the appearance of the dichroism (with respect to inversion of the target orientation) is to be expected since for high energies and small momentum transfer the charged-particle scattering is intimately related to photoabsorption process via the dipolar limit. Very recent advances in coincidence detection techniques have rendered possible the investigation of the chiral two-electron continuum following the electron-impact ionisation of laser-oriented targets [58,59]. This is particularly interesting, for such studies offer an opportunity to zoom in the chirality transfer from a bound system onto a correlated electron pair and to compare with the case where the chirality of the electron pair had been put into the system by an external perturbation, as is the case for double-electron emission upon the absorption of a circularly polarised photon. Thus in Section 4, we envisage theoretically, using a tensorial analysis, the physical and mathematical structure of the chiral electron-pair continuum states achieved upon electron-impact ionisation of oriented atoms. Emphasis is put on the symmetry analysis and on the role of the orientation transfer from the initial target to the two correlated electrons. The formal development is complemented with numerical studies and the theoretical results are contrasted against recent experimental finding. Finally, we conclude this article by a summary and a brief outlook of future directions. Unless otherwise stated we use atomic units throughout.

2. One-electron photoemission

In this section we present compactly the main feature of the photoelectron spectra in single photoemission and point out the reason for the appearance of dichroism, i.e. a difference in the

spectrum when the helicity of the photon is inverted. At a first glance one might reject a dichroism in consequence of Yang's theorem [15]. According to this theorem the angular distribution of the photoelectrons, i.e. the cross-section for the emission of a photoelectron under a solid angle Ω, is described by

$$\frac{\mathrm{d}\sigma}{\mathrm{d}\Omega} = \frac{\sigma_0}{4\pi}[1 + \beta P_2(\cos\theta)] \,, \tag{2.1}$$

where σ_0 is the total cross section, β is the asymmetry parameter, P_2 is the second Legendre polynomial and θ is the angle between the photoelectron momentum and the light propagation direction (for circular polarisation) or between the photoelectron momentum and the electric field (for linear polarisation). In particular, we see that the helicity of the light does not enter into Eq. (2.1), i.e. there is no circular dichroism. Yang's formula however holds only for unpolarised target atoms and provided the spin of the photoelectron is not being observed. As stated in the introduction, the situation changes when the spin of the electron is resolved or when the target atoms are polarised, e.g., if the atomic target is polarised with $\hat{\boldsymbol{a}}$ being a unit vector along its quantisation axis, the angular distribution of the photoelectrons has the general form Ref. [23]

$$\frac{\mathrm{d}\sigma}{\mathrm{d}\Omega} = 4\pi^2\alpha a_0^2\omega(-1)^{1+q}\sum_{LKY}\langle 1q1-q\,|\,Y0\rangle\rho_{K0}B(L,K,Y)\mathscr{Y}_{Y0}^{LK}(\hat{\boldsymbol{p}},\hat{\boldsymbol{a}}) \,. \tag{2.2}$$

Here α is the fine-structure constant, a_0 is the Bohr radius, ω is the frequency of the light and $\hat{\boldsymbol{p}}$ is the emission direction of the photoelectron. q quantifies the polarisation state of the light, i.e. $q = \pm 1$ indicates right/left circular polarisation whereas $q = 0$ means linear polarisation. In Eq. (2.2) we assumed the hyperfine structure of the target to be resolved and to be labelled by the quantum numbers F_0. The population of hyperfine states of the target is conveniently described by the density matrix $\rho_{F_0M_0F_0M_0'}$ (cf. Ref. [60]). In Eq. (2.2) the density matrix has been expressed through its state multipoles ρ_{K0} (see Ref. [60] for details) via the relation

$$\rho_{F_0M_0F_0M_0'} = \sum_K (-1)^{K-F_0-M_0}\sqrt{\frac{4\pi}{2K+1}}\langle F_0 - M_0F_0M_0'|KM_0' - M_0\rangle\rho_{K0}Y_{KM_0'-M_0}(\hat{\boldsymbol{a}}) \,, \tag{2.3}$$

where Y_{KQ} is a standard spherical harmonics. The angular function $\mathscr{Y}_{Y0}^{LK}(\hat{\boldsymbol{p}},\hat{\boldsymbol{a}})$ in Eq. (2.2) is the result of coupling two spherical harmonics associated with the directions $\hat{\boldsymbol{p}}$ and $\hat{\boldsymbol{a}}$ and will be discussed in more details in the next sections. In Eq. (2.2) the generalised asymmetry parameters B appear. Those are given by

$$B(L,K,Y) = (2F_0+1)\begin{Bmatrix} K & J_0 & J_0 \\ I & F_0 & F_0 \end{Bmatrix}$$

$$\sum_{ljJl'j'J'}(-1)^{J_0+I+F_0+J_f+J-\frac{1}{2}}\sqrt{[(2l+1)(2l'+1)(2j+1)(2j'+1)}$$

$$(2J+1)(2J'+1)\langle l0l'0|L0\rangle \begin{Bmatrix} L & J' & J \\ J_f & j & j' \end{Bmatrix} \begin{Bmatrix} L & j' & j \\ \frac{1}{2} & l & l' \end{Bmatrix}$$
$$\begin{Bmatrix} L & J & J' \\ K & J_0 & J_0 \\ Y & 1 & 1 \end{Bmatrix} \left\langle J_f\left(l\frac{1}{2}\right); J\|r\|J_0 \right\rangle \left\langle J_f\left(l'\frac{1}{2}\right) j'; J'\|r\|J_0 \right\rangle^* . \tag{2.4}$$

Here the familiar definition of angular momentum quantum numbers is used, i.e. L is the total orbital angular momentum, J is the total electronic angular momentum with coupling scheme $(LS)J$, I is the nuclear spin, and F is the overall angular momentum with coupling scheme $(JI)F$.

From the symmetry properties of the Clebsch–Gordan coefficients [cf. Eq. (2.2)] it follows that the term $Y = 1$ describes a circular dichroism provided B and $\mathcal{Y}$ are non-vanishing. In the simplest case ($K = L = 1$) the corresponding angular function is given by $\mathcal{Y}^{11}_{10}(\hat{\boldsymbol{p}}, \hat{\boldsymbol{a}}) \propto \hat{\boldsymbol{p}} \times \hat{\boldsymbol{a}}$. This means that the circular dichroism can be observed provided the vectors $\hat{\boldsymbol{p}}$ and $\hat{\boldsymbol{a}}$ are linearly independent (i.e. not (anti)parallel). The dichroism should be largest if the photoelectron is observed perpendicular to the quantisation axis $\hat{\boldsymbol{a}}$ of the target. A finite value of B requires $J_0 \geq \frac{1}{2}$. The total cross-section does not reveal any dichroism since the angular integration over the emission direction of the photoelectron selects $L = 0$. The physical origin of the circular dichroism in this case is the existence of an initial target orientation (described by $K = 1$ and realised for instance by optical pumping). In course of the photoionisation process this orientation is transferred to the photoelectron continuum. An absence of the orientation of the target will destroy the dichroic effect, as is the case for isotropic target. However, as we will see in the next section the situation is different when two photoelectrons are emitted and simultaneously detected.

3. Production of chiral electron pairs by one-photon absorption

In this section we focus on the direct emission of correlated electron pairs with chirality as an internal degree of freedom. By means of a general mathematical analysis we discuss how the chirality of the photon (absorbed by the electron pair) is transferred to the two coupled electrons and in which way the electronic correlation is interfering with this new feature of the electrons. A numerical analysis with various levels of sophistication allows some insights in the actual values of this chiral effect and in its dependence on the energy of the photon. The different theoretical approaches are contrasted against the experimental findings and the exact analytical results.

The case of double ionisation with one linear polarised photon will not be discussed here unless it is of direct relevance to the chiral effects. The interested reader is referred to the excellent recent review article [54] and to the references therein.

3.1. General analytical properties of the circular dichroism in one-photon two-electron transitions

At a fixed light frequency ω, the energy- and angle-resolved cross-section W for the one-photon two-electron transition can be written in the form (see for instance [61,62])

$$W(\Omega_a, \Omega_b, E_a) = C \sum_{M_f} \frac{1}{2J_i + 1} \sum_{M_i} |\langle \Psi^-_{k_a,k_b} | \hat{\varepsilon} \cdot \boldsymbol{D} | \Phi_i \rangle|^2 . \tag{3.1}$$

Here the momenta of the two escaping electrons are labelled by $\boldsymbol{k}_a$ and $\boldsymbol{k}_b$ whereas the E_γ is the incident radiation energy and $C = 4\pi^2\alpha a_0^2 E_\gamma k_a k_b$. The many-body dipole operator $\boldsymbol{D} = \sum_n \boldsymbol{d}_n$ (in the length form) can be expressed in terms of the single particle dipole operator $\boldsymbol{d}_i$. The light polarisation vector is referred to by $\hat{\varepsilon}$. In Eq. (2) we average over the initial magnetic sublevels M_i, and sum over the magnetic sublevels M_f of the photoion. If we define E_a and E_b as the energies of the escaping electrons and $E = E_a + E_b$ as their total kinetic energy, Eq. (3.1) can be rewritten in the form

$$W(\boldsymbol{k}_a, \boldsymbol{k}_b) = C' \sum_{M_\mathrm{f}} \langle \Psi^-_{\boldsymbol{k}_a,\boldsymbol{k}_b} | \Delta S \Delta^\dagger | \Psi^-_{\boldsymbol{k}_a,\boldsymbol{k}_b} \rangle \,, \tag{3.2}$$

where $C' = 4\pi^2\alpha a_0^2 E_\gamma$ and $\Delta = \hat{\varepsilon}\cdot\boldsymbol{D}$ is the two-particle *photon dipole operator*. The operator S is given by

$$S = \frac{1}{2J_\mathrm{i}+1} \sum_{M_\mathrm{i}} |\Phi_\mathrm{i}\rangle\langle\Phi_\mathrm{i}| \delta(E_\gamma + \varepsilon_\mathrm{i} - E) \,. \tag{3.3}$$

Here ε_i is the (negative) binding energy of the two electrons in the initial state. Eq. (3.3) quantifies the density of occupied states. In the context of many-particle theory S is usually expressed in terms of the imaginary part of the Green function G of the occupied states (this is valid for an infinite two-particle life time)

$$-\frac{1}{\pi} \operatorname{Im} G(E) = \sum_{M_\mathrm{i}} |\Phi_\mathrm{i}\rangle \delta(E - \varepsilon_\mathrm{i}) \langle \Phi_\mathrm{i}| \,. \tag{3.4}$$

Using Eq. (3.4) the cross-section (3.2) then reads

$$W(\boldsymbol{k}_a, \boldsymbol{k}_b) = -\frac{C''}{\pi} \sum_{M_\mathrm{f}} \langle \Psi^-_{\boldsymbol{k}_a,\boldsymbol{k}_b} | \Delta \operatorname{Im} G(E - E_\gamma) \Delta^\dagger | \Psi^-_{\boldsymbol{k}_a,\boldsymbol{k}_b} \rangle \,. \tag{3.5}$$

Most of modern theories of single photoemission from extended systems relies on the so-called one-step photoelectron current formula that has been derived by Caroli et al. [63]. This formula rests on the non-equilibrium Green function formalism. The Caroli formula states that upon the absorption of a one low-energy photon by an electronic system, the photoelectron current $J(\boldsymbol{k})$ can be calculated as $J(\boldsymbol{k}) = -(1/\pi)\langle\psi_{\boldsymbol{k}}|\Delta \operatorname{Im} G(E_k - E_\gamma)\Delta^\dagger|\psi_{\boldsymbol{k}}\rangle$ where $|\psi_{\boldsymbol{k}}\rangle$ is the excited (final) state of the electron with a wave vector $\boldsymbol{k}$ and energy $E_{\boldsymbol{k}}$. Thus, relation (3.5) is nothing but the exact analogue of the Caroli formula for the two-particle current [64]. Hence, the conclusions drawn in the subsequent sections are readily generalised to extended systems, such as solids and surfaces [67]. A thorough discussion of the many-particle currents is beyond the scope of the present work, some details can be found in Refs. [64–66].

For the production of chiral electrons it is decisive that the target (prior to the absorption process) is randomly oriented, i.e. the chirality of the electron pair is imparted by the photon field. This isotropy of the target state ensures that the projection operator S (as given by Eq. (3.3)) is a scalar. Therefore the operator $\boldsymbol{D}' = S\boldsymbol{D}$ is a polar vector operator with respect to overall rotations. It should be emphasised, however, that this conclusion would not be true if the initial state were oriented, as is the case in the previous and the next section.

Our strategy to extract formal analytical expressions for the circular dichroism is based on a decoupling of geometrical from dynamical effects. This is achieved by expressing the vectors $\hat{\varepsilon}$, $\hat{\varepsilon}^*$, $\boldsymbol{D}$ and $\boldsymbol{D}'$ as spherical tensors of rank one and employing a tensorial re-coupling scheme that formally resembles the one used by Fano and Macek [68] in their polarisation analysis of the dipole radiation emitted from oriented and aligned targets. The product $(\hat{\varepsilon}\cdot\boldsymbol{D})(\hat{\varepsilon}^*\cdot\boldsymbol{D}')$ can be expanded symbolically in the outer and inner products as

$$(\hat{\varepsilon}\cdot\boldsymbol{D})(\hat{\varepsilon}^*\cdot\boldsymbol{D}') = \tfrac{1}{3}(\boldsymbol{D}\cdot\boldsymbol{D}') + \tfrac{1}{2}(\hat{\varepsilon}\times\hat{\varepsilon}^*)\cdot(\boldsymbol{D}\times\boldsymbol{D}') + T_2(\hat{\varepsilon},\hat{\varepsilon}^*)\cdot T_2(\boldsymbol{D},\boldsymbol{D}')\,, \tag{3.6}$$

where $T_2(x,y)$ stands for a tensor of rank 2 formed from the two spherical tensors of rank one (the components of $T_2(x,y)$ are given by the formula $T_{2,Q}(x,y) = \sum_{p,q}\langle 1p1-q|2Q\rangle x_{1,p}y_{1,q}$ where $\langle\cdots|\cdots\rangle$ denotes the Clebsch–Gordon coefficients).

A change of the light helicity corresponds to a replacement of $\hat{\varepsilon}$ by its complex conjugate $\hat{\varepsilon}^*$. The vector product term in relation (3.6) is the only term being odd with respect to this replacement. This term is therefore the quantity sensitive to inversion of the helicity of the photon.

In what follows we make the convention $\hat{\varepsilon}(\hat{\varepsilon}^*)$ to describe left (right) circularly polarised light. Furthermore, we denote the difference of the cross-sections for left and right circularly polarised light as the circular dichroism (hereafter referred to by CD), i.e. $\mathrm{CD} = W(\sigma^+) - W(\sigma^-)$ where σ^+ (σ^-) stands for the helicity of the left (right) hand circularly polarised photon. Further simplification is achieved by assuming the z-axis to be the direction $\boldsymbol{k}$ of the incident light. With $\hat{\varepsilon} = \frac{1}{\sqrt{2}}(1,\mathrm{i},0)$ and $\hat{\varepsilon}\times\hat{\varepsilon}^* = -\mathrm{i}\hat{\boldsymbol{k}}$ we conclude for the dichroism the relation

$$\mathrm{CD}(\sigma^+,\boldsymbol{k}_a,\boldsymbol{k}_b) = -\mathrm{i}C\sum_{M_f}\langle\Psi^-_{\boldsymbol{k}_a,\boldsymbol{k}_b}|[\boldsymbol{D}\times\boldsymbol{D}']_0|\Psi^-_{\boldsymbol{k}_a,\boldsymbol{k}_b}\rangle\,, \tag{3.7}$$

where the index *zero* refers to the z-component, i.e. $[\boldsymbol{D}\times\boldsymbol{D}']_0 = [\boldsymbol{D}\times\boldsymbol{D}']\cdot\hat{\boldsymbol{k}}$. This identifies the CD as an expectation value of the pseudovector operator $\boldsymbol{D}\times\boldsymbol{D}'$. We note in this context that, for a general N electron system, the dichroism CD cannot be regarded as an orientation in the sense of Fano and Macek [68]. This is because, in contrast to the cases treated in Ref. [68], the present final state is generally *not* an eigenstate of total angular momentum (except for a ^1S initial state).

So far this formal development applies as it stands for single photoionisation. However, as we mentioned earlier, according to Yang's formula [15] the CD should vanish in case of single photoemission. Thus, it is instructive to show (a) that our mathematical analysis is consistent with Yang's formula and (b) that the CD is generally finite for many-electron emission.

To this end we define the circular dichroism δ in the case of single photoemission as the correspondence to Eq. (3.7), namely

$$\delta \propto \langle\psi_{\boldsymbol{k}}|[\boldsymbol{D}\times\boldsymbol{D}']_0|\psi_{\boldsymbol{k}}\rangle\,. \tag{3.8}$$

As we will show δ vanishes due to conservation of parity. This is deduced from the partial wave expansion

$$|\psi_{\boldsymbol{k}}\rangle = \sum_{lm}|\psi_{lm}\rangle C_{lm}(\hat{\boldsymbol{k}}) \tag{3.9}$$

where $C_{lm}(\hat{\boldsymbol{k}})$ is a spherical harmonic in the notation of Ref. [69]. Upon substituting (3.9) into the expression for δ, applying the Wigner–Eckart theorem, and performing the sum over m,

we conclude

$$\delta \propto \sum_{l'l} (-)^{l'} \begin{pmatrix} l' & l & 1 \\ 0 & 0 & 0 \end{pmatrix} C_{10}(\hat{\boldsymbol{k}}) \langle \psi_{l'} \| \boldsymbol{D} \times \boldsymbol{D}' \| \Psi_l^- \rangle \,. \tag{3.10}$$

The symbol

$$\begin{pmatrix} j_1 & j_2 & j_3 \\ m_1 & m_2 & m_3 \end{pmatrix}$$

is a $3-j$ symbol. The point is now that only even or only odd values of l and l' contribute because of parity conservation. We assume here that the initial state is a parity eigenstate which is usually the case. The $3-j$ symbol in (9) is then equal to zero because $l'+l+1 =$ odd. Moreover $l'=l$ because $(l', l, 1)$ satisfy a triangular relation.

In contrast to single photoemission, for one-photon double ionisation (PDI) parity conservation does *not* imply the absence of dichroism. To show this we proceed as in the case of single photoionisation and expand the final state into partial waves,

$$|\Psi^-_{\boldsymbol{k}_a \boldsymbol{k}_b}\rangle = \sum_{l_a l_b lm} |\Psi^-_{l_a l_b lm}\rangle B^{l_a l_b}_{lm}(\hat{\boldsymbol{k}}_a, \hat{\boldsymbol{k}}_b) \,. \tag{3.11}$$

The bipolar spherical harmonics $B^{l_a l_b}_{lm}(\hat{\boldsymbol{k}}_a, \hat{\boldsymbol{k}}_b)$ [69] are basically the tensor products of two spherical harmonics (with appropriate normalisation) and are given by

$$B^{l_1 l_2}_{lm}(\hat{\boldsymbol{x}}, \hat{\boldsymbol{y}}) = \sum_{m_1 m_2} \langle l_1 m_1 l_2 m_2 \,|\, lm\rangle C_{l_1 m_1}(\hat{\boldsymbol{x}}) C_{l_2 m_2}(\hat{\boldsymbol{y}}) \,.$$

Parity conservation in (10) implies that $l_a + l_b$ is either even or odd. We substitute the partial wave expansion (3.11) into (3.7) and apply the Clebsch–Gordan series for bipolar harmonics [70]

$$B^{l_a l_b}_{lm}(\hat{\boldsymbol{a}}, \hat{\boldsymbol{b}}) B^{l'_a l'_b}_{l'm'}(\hat{\boldsymbol{a}}, \hat{\boldsymbol{b}})^* = (-)^{l_a + l_b + l' + m'} \sqrt{(2l+1)(2l'+1)}$$

$$\sum_{L_a L_b K Q} (2L_a+1)(2L_b+1) \begin{pmatrix} l_a & l'_a & L_a \\ 0 & 0 & 0 \end{pmatrix} \begin{pmatrix} l_b & l'_b & L_b \\ 0 & 0 & 0 \end{pmatrix} \begin{Bmatrix} l & l' & K \\ l_a & l'_a & L_a \\ l_b & l'_b & L_b \end{Bmatrix}$$

$$\langle lml' - m' \,|\, KQ\rangle B^{L_a L_b}_{KQ}(\hat{\boldsymbol{a}}, \hat{\boldsymbol{b}}) \,. \tag{3.12}$$

In the final state we couple the angular momentum J_f of the ion with the angular momentum l of the electron pair to the resultant J. Applying the Wigner–Eckart theorem, the summation over all magnetic quantum numbers can then be performed, and we find for the dichroism

$$\mathrm{CD}(\sigma^+, \boldsymbol{k}_a, \boldsymbol{k}_b) = -\mathrm{i} \sum_{L_a L_b} \gamma_{L_a L_b} B^{L_a L_b}_{10}(\hat{\boldsymbol{k}}_a, \hat{\boldsymbol{k}}_b) \tag{3.13}$$

with

$$\gamma_{L_a L_b} = C \sum_{l_a l_b l l'_a l'_b l' J J'} (-)^{l_a + l_b + l' + J' + J_f + 1} (2J' + 1)(2L_a + 1)(2L_b + 1)$$
$$\sqrt{\frac{(2l+1)(2l'+1)}{3}} \begin{pmatrix} l_a & l'_a & L_a \\ 0 & 0 & 0 \end{pmatrix} \begin{pmatrix} l_b & l'_b & L_b \\ 0 & 0 & 0 \end{pmatrix} \begin{Bmatrix} l' & J_f & J' \\ J & 1 & l \end{Bmatrix} \begin{Bmatrix} l & l' & 1 \\ l_a & l'_a & L_a \\ l_b & l'_b & L_b \end{Bmatrix}$$
$$\langle J_f(l'_a l'_b) l'; J' || \boldsymbol{D} \times \boldsymbol{D}' || J_f(l_a l_b) l; J \rangle \,. \tag{3.14}$$

To simplify further Eqs. (3.13) and (3.14) we remark that, usually, in a photoionisation experiment the initial target as well as the final ion are in parity eigenstates. The pair of escaping electrons in one-photon double ionisation will therefore be in a parity eigenstate with parity $\pi = (-)^{l_a + l_b}$ where l_a and l_b are the orbital angular momenta of the electrons. Since the two electrons are exchanging energy and momentum the one-electron angular momentum states are not useful to characterise the pair's states. In fact, many pairs of angular momenta (l_a, l_b) will contribute to the two-electron continuum state such that $l_a + l_b$ is either even or odd. For example, double photoionisation of He or H^- in the ground state (^1S) leads to the $^1P^{\text{odd}}$ symmetry with configurations $(l_a, l_b) = (s,p),(p,d),(d,f),\ldots$.

From (3.14) it follows that only pairs of (L_a, L_b) with $L_a = L_b$ contribute to the circular dichroism (3.13). Further inspection of the $3-j$ symbols in (3.14) reveals that finite coefficients require the following relation be fulfilled:

$$l_a + l'_a + L_a = \text{even} \,,$$
$$l_b + l'_b + L_b = \text{even} \,.$$

We add these two equations and conclude $L_a + L_b = \text{even}$ because $l_a + l_b$ and $l'_a + l'_b$ are both either even or odd. Then we see from the $9-j$ symbol that the three numbers $(1, L_a, L_b)$ satisfy a triangular relation. Since the case $L_a = L_b \pm 1$ leads to odd values of $L_a + L_b$ we arrive at $L_a = L_b$. Therefore, Eq. (3.13) can be simplified as

$$\text{CD}(\sigma^+, \boldsymbol{k}_a, \boldsymbol{k}_b) = -\mathrm{i} \sum_L \gamma_{LL} B_{10}^{LL}(\hat{\boldsymbol{k}}_a, \hat{\boldsymbol{k}}_b) \,. \tag{3.15}$$

Since only the diagonal elements γ_{LL} contribute to Eq. (3.15) one might expect that the dichroism is less sensitive a quantity to the description of the scattering dynamics than the cross-sections. As discussed below, the CD carries particular information related to phase differences of the optical transition amplitudes. A measurement of the CD alone is not sufficient for a complete description of the photodouble-ionisation (PDI) process.

3.2. Propensity rules for the circular dichroism

As any physical observable, the CD must be invariant under an exchange of the two electrons, i.e.

$$\text{CD}(\sigma^+, \boldsymbol{k}_a, \boldsymbol{k}_b) = \text{CD}(\sigma^+, \boldsymbol{k}_b, \boldsymbol{k}_a) \,. \tag{3.16}$$

In addition as clear from the definition of the dichroism the CD is odd with respect to inversion of the helicity of the photon, i.e.

$$\mathrm{CD}(\sigma^+, \boldsymbol{k}_a, \boldsymbol{k}_b) = -\mathrm{CD}(\sigma^-, \boldsymbol{k}_a, \boldsymbol{k}_b)\ . \tag{3.17}$$

From Eqs. (3.16) and (3.17) we conclude

$$\mathrm{CD}(\sigma^+, \boldsymbol{k}_a, \boldsymbol{k}_b) = -\mathrm{CD}(\sigma^-, \boldsymbol{k}_b, \boldsymbol{k}_a) \tag{3.18}$$

this means a grand reflection of the experimental set-up results in a sign change of the CD (the CD is a pseudoscalar in the laboratory coordinate frame). To analyse the behaviour of the CD when the electrons' energies and the solid angles Ω_a, Ω_b are the relevant parameters we have to discuss the angular functions $B_{10}^{LL}(\hat{\boldsymbol{k}}_a, \hat{\boldsymbol{k}}_b)$. These functions are decisive for the angular behaviour of the CD as seen from Eq. (3.15). They are explicitly given by

$$B_{10}^{LL}(\hat{\boldsymbol{k}}_a, \hat{\boldsymbol{k}}_b) = \sum_M \langle LML - M \,|\, 10\rangle C_{LM}(\hat{\boldsymbol{k}}_a) C_{L-M}(\hat{\boldsymbol{k}}_b)\ . \tag{3.19}$$

From this equation we deduce the following properties:

1. $B_{10}^{LL}(\hat{\boldsymbol{k}}_a, \hat{\boldsymbol{k}}_b)$ are purely imaginary. This follows from the relation $C_{LM}(\hat{\boldsymbol{x}})^* = (-)^M C_{L-M}(\hat{\boldsymbol{x}})$ for spherical harmonics and the symmetry formula $\langle L - MLM \,|\, 10\rangle = -\langle LML - M \,|\, 10\rangle$ for Clebsch–Gordan coefficients. The dichroism CD is a difference of cross-sections and as such must be real. Therefore, we conclude that the coefficients γ_{LL} in (14) are real as well.
2. $B_{10}^{LL}(\hat{\boldsymbol{k}}_a, \hat{\boldsymbol{k}}_b)$ are parity-even in the solid angles associated with the momenta $\boldsymbol{k}_a, \boldsymbol{k}_b$ of the two photoelectrons, i.e. $B_{10}^{LL}(-\hat{\boldsymbol{k}}_a, -\hat{\boldsymbol{k}}_b) = B_{10}^{LL}(\hat{\boldsymbol{k}}_a, \hat{\boldsymbol{k}}_b)$ which follows from the parity of spherical harmonics given by $C_{LM}(-\hat{\boldsymbol{x}}) = (-)^L C_{LM}(\hat{\boldsymbol{x}})$.
3. From the symmetry of Clebsch–Gordan coefficients, we deduce furthermore that Eq. (3.19) is odd with respect to exchange of the electrons, i.e. $B_{10}^{LL}(\hat{\boldsymbol{k}}_b, \hat{\boldsymbol{k}}_a) = -B_{10}^{LL}(\hat{\boldsymbol{k}}_a, \hat{\boldsymbol{k}}_b)$. This relation implies that:
4. $B_{10}^{LL}(\hat{\boldsymbol{k}}_a, \hat{\boldsymbol{k}}_b)$ vanishes when the two electrons escape in the same direction and, due to relation (3.16), the functions γ_{LL} has to satisfy the condition

$$\gamma_{LL}(k_a, k_b) = -\gamma_{LL}(k_b, k_a)\ . \tag{3.20}$$

   This leads to a vanishing dichroism for emission of two electrons with equal energies.
5. B_{10}^{LL} vanishes when the electrons recede in a back-to-back configuration ($\hat{\boldsymbol{k}}_b \,||\, -\hat{\boldsymbol{k}}_a$). This is concluded by considering the quantity

$$B_{10}^{LL}(\hat{\boldsymbol{x}}, \hat{\boldsymbol{x}}) = \sum_M \langle LML - M \,|\, 10\rangle C_{LM}(\hat{\boldsymbol{x}}) C_{L-M}(\hat{\boldsymbol{x}}) \tag{3.21}$$

   and substituting the expansion

$$C_{LM}(\hat{\boldsymbol{x}}) C_{L-M}(\hat{\boldsymbol{x}}) = \sum_K \langle LML - M \,|\, K0\rangle \langle L0L0 \,|\, K0\rangle C_{K0}(\hat{\boldsymbol{x}})\ . \tag{3.22}$$

   The orthogonality of Clebsch–Gordan coefficients selects then the only value $K = 1$ for which, however, $\langle L0L0 \,|\, 10\rangle = 0$. For $\hat{\boldsymbol{k}}_b = -\hat{\boldsymbol{k}}_a$ we use $C_{LM}(-\hat{\boldsymbol{x}}) = (-)^L C_{LM}(\hat{\boldsymbol{x}})$ and repeat the arguments above.

6. The CD vanishes if the direction of the incident light $\hat{\boldsymbol{k}}$ and the electrons' vector momenta $\boldsymbol{k}_a, \boldsymbol{k}_b$ are linearly dependent. The above consideration assumes a co-ordinate frame with the z-axis being along $\hat{\boldsymbol{k}}$. Now let us select an arbitrary direction of $\hat{\boldsymbol{k}}_a$ described by the polar angles θ_a, φ_a. If the three vectors $\hat{\boldsymbol{k}}$ and $\boldsymbol{k}_a, \boldsymbol{k}_b$ are linearly dependent the spherical position of $\hat{\boldsymbol{k}}_b$ is determined by $\theta_b, \varphi_b = \varphi_a + N\pi$ with $N =$ integer. The product of phase factors of the spherical harmonics is then real. For this reason also the bipolar harmonics (3.19) are real which contradicts the prediction that they are purely imaginary, except for the case when they are equal to zero.
7. The CD vanishes in a non-coincidence experiment, i.e. if we integrate over one of the directions $\hat{\boldsymbol{k}}_a$ or $\hat{\boldsymbol{k}}_b$. This follows directly from the orthogonality of spherical harmonics and $L \geq 1$. Thus, one can interpret the CD as a feature which is shared by the correlated chiral electron pair, exclusively. If one of the electrons of the chiral pair is not detected the CD is destroyed. This fact together with the exact geometrical propensity rules exposed above makes the CD a predestine candidate for the study of entanglement in quantum systems.

3.3. Alternative routes to the circular dichroism

As shown by an elegant mathematical analysis [40,48,49], the propensity rules of CD, as listed above, appear naturally from the parameterisation of the cross-section (3.1) as

$$W(\Omega_a, \Omega_b, E_a) = \sigma_0 + \xi\sigma_1 \hat{\boldsymbol{k}}\cdot(\hat{\boldsymbol{k}}_a \times \hat{\boldsymbol{k}}_b) + \sigma_2\{3\mathrm{Re}[(\hat{\varepsilon}\cdot\hat{\boldsymbol{k}}_a)(\hat{\varepsilon}^*\cdot\hat{\boldsymbol{k}}_b)] - \hat{\boldsymbol{k}}_a\cdot\hat{\boldsymbol{k}}_b\} + \sigma_2^{(1)}(3|\hat{\varepsilon}\cdot\hat{\boldsymbol{k}}_a| - 1) + \sigma_2^{(2)}(3|\hat{\varepsilon}\cdot\hat{\boldsymbol{k}}_b| - 1)\,. \tag{3.23}$$

Here ξ is the degree of circular polarisation and the five dependent parameters $\sigma_0, \sigma_1, \sigma_2, \sigma_2^{(1/2)}$ depend on the energies of the ejected electrons and on the mutual angle between the emission directions of the two electrons. It is the term $\xi\sigma_1 \hat{\boldsymbol{k}}\cdot(\hat{\boldsymbol{k}}_a \times \hat{\boldsymbol{k}}_b)$ in Eq. (3.23) that describes the CD. The triple product in this term encompasses, basically all the geometrical properties of the CD. The dynamical features of the CD are contained in the function σ_1. The numerical evaluation of this function requires a dynamical model for the motion of the electron pair in the presence of the field of the atom. Such models will be presented and discussed in the forthcoming sections.

In Ref. [40] Eq. (3.23) has been derived using a reduction scheme for bipolar harmonics. Another approach that proved very useful in analysing the PDI process relies on the Wannier–Peterkop–Rau theory [71–73], as formulated in Ref. [74]. To illustrate the use of this theory we consider an initial state of the electron pair with a $^1S^{\mathrm{even}}$ symmetry. Thus, the two coupled photoelectrons go over into a $^1P^{\mathrm{odd}}$ symmetry with magnetic quantum numbers $M = \pm 1$ upon the absorption of a circularly polarised photon. According to Table 3 of Ref. [74] the general form of the final state wave function reads

$$\Psi_{M=\pm 1} = \pm F^{\mathrm{g}}\{\sin\vartheta_a \mathrm{e}^{\pm \mathrm{i}\varphi_a} + \sin\vartheta_b \mathrm{e}^{\pm \mathrm{i}\varphi_b}\} \pm F^{\mathrm{u}}\{-\sin\vartheta_a \mathrm{e}^{\pm \mathrm{i}\varphi_a} + \sin\vartheta_b \mathrm{e}^{\pm \mathrm{i}\varphi_b}\}\,, \tag{3.24}$$

where the functions F^{g} and F^{u} depend on the rotationally invariant positions r_a, r_b of the two electrons and the inter-electronic angle $\vartheta_{ab} = \cos^{-1}(\hat{r}_a\cdot\hat{r}_b)$. In Eq. (3.24) the angles ϑ_a, ϑ_b and φ_a, φ_b are the polar and azimuthal angles of $\boldsymbol{r}_a$ and $\boldsymbol{r}_b$ in a frame with the z-axis along the direction of the photon beam.

The functions F^{g} and F^{u} are, respectively, symmetric and antisymmetric under an interchange $\boldsymbol{r}_a \leftrightarrow \boldsymbol{r}_b$. To arrive at the angular structure of the PDI cross-section one employs the asymptotic

form of (3.24) which yields

$$W(\Omega_a, \Omega_b, E_a)|_{M=\pm 1} = |a_g\{\sin\theta_a + \sin\theta_b e^{\pm i\varphi}\} + a_u\{-\sin\theta_a + \sin\theta_b e^{\pm i\varphi}\}|^2 . \tag{3.25}$$

The complex functions $a_g(E_a, E_b, \theta_{ab})$ and $a_u(E_a, E_b, \theta_{ab})$ are given by the asymptotic behavior of quantities F^g and F^u in case the azimuthal and polar angles $\phi_{a/b}$ and $\theta_{a/b}$ are now being associated with the directions of the momenta $\boldsymbol{k}_a$ and $\boldsymbol{k}_b$ as measured with respect to a z direction pointing into the photon beam direction, and φ is given by $\varphi = \phi_b - \phi_a$. In the particular case of symmetric energy sharing ($E_a = E_b$) the asymptotic form of the final state is symmetric in $\boldsymbol{r}_a \leftrightarrow \boldsymbol{r}_b$, and this causes the second term in (3.25) to vanish, i.e. $a_u = 0$.

The CD is derived from Eq. (3.25) to be

$$\mathrm{CD} = 8\ \mathrm{Im}(a_g a_u^*)\sin\theta_a \sin\theta_b \sin\varphi . \tag{3.26}$$

Again we verify from this relation the propensity rules for the CD, e.g., there is no dichroism if $\boldsymbol{k}_a$ and $\boldsymbol{k}_b$ are linearly dependent, i.e. if ($\varphi = 0$ or π). The CD vanishes in symmetric energy sharing ($E_a = E_b$) because in this case $a_u = 0$. Eq. (3.26) suggests first rough estimate for the value of the CD, namely the CD is largest for $\theta_a = \theta_b = \varphi = \pi/2$ (note, however, that the gerade and the ungerade amplitudes depend on the inter-electronic angle).

The angular dependence of CD as given in (3.26) is consistent with the structure of the CD as given by Eq. (3.15) in terms of the bipolar harmonics. In fact, it is straightforward to show that the angular part $\sin\theta_a \sin\theta_b \sin\varphi$ of Eq. (3.26) can be written as

$$\sin\theta_a \sin\theta_b \sin\varphi = -2iB_{10}^{11}(\hat{\boldsymbol{k}}_a, \hat{\boldsymbol{k}}_b) = (-2i)\frac{i}{\sqrt{2}}\hat{\boldsymbol{k}}\cdot(\hat{\boldsymbol{k}}_a \times \hat{\boldsymbol{k}}_b) . \tag{3.27}$$

Furthermore, one can verify that the portion B_{10}^{11} is contained in all angular functions B_{10}^{LL}. In other words, B_{10}^{LL} can be written as $B_{10}^{LL} = B_{10}^{11}\tilde{B}_{10}^{LL} = (i/\sqrt{2})\hat{\boldsymbol{k}}\cdot(\hat{\boldsymbol{k}}_a \times \hat{\boldsymbol{k}}_b)\tilde{B}_{10}^{LL}$. This relation allows to rewrite Eq. (3.15) in the form

$$\mathrm{CD}(\sigma^+, \boldsymbol{k}_a, \boldsymbol{k}_b) = \frac{i}{\sqrt{2}}\sum_L \gamma_{LL}\tilde{B}_{10}^{LL}\hat{\boldsymbol{k}}\cdot(\hat{\boldsymbol{k}}_a \times \hat{\boldsymbol{k}}_b) . \tag{3.28}$$

Hence, all three forms of the CD given by Eqs. (3.15), (3.23) and (3.26) have the same angular structure. In fact, the general parameterisation (3.23) can be expressed in terms of the gerade and the ungerade amplitudes a_g and a_u as [48,49]

$$\begin{aligned}
\sigma_0 &= \sigma_2^{(1)} + \sigma_2^{(2)} + \sigma_2\cos\theta_{ab} ,\\
\sigma_1 &= -i[a_g a_u^* - a_g^* a_u] ,\\
\sigma_2^{(1)} &= \tfrac{1}{3}\{|a_g|^2 + (a_g a_u^* + a_g^* a_u) + |a_u|^2\} ,\\
\sigma_2^{(2)} &= \tfrac{1}{3}\{|a_g|^2 - (a_g a_u^* + a_g^* a_u) + |a_u|^2\} ,\\
\sigma_2 &= \tfrac{2}{3}\{|a_g|^2 - |a_u|^2\} ,\\
\sigma_0 &= \sigma_2^{(1)} + \sigma_2^{(2)} + \sigma_2\cos\theta_{ab} .
\end{aligned} \tag{3.29}$$

3.4. The circular dichroism and the role of the Pauli principle

The angular dependence of the CD in the laboratory frame, as given by Eqs. (3.28), (3.23) and (3.26), allows the interpretation that the three vectors $\hat{\boldsymbol{k}}_a, \hat{\boldsymbol{k}}_b$ and $\hat{\boldsymbol{k}}$ span a (generally non-orthogonal) co-ordinate system $\mathscr{S}$ in space. An inversion of the helicity of the photon corresponds to an inversion of the orientation of $\mathscr{S}$. Such an inversion of the orientation of $\mathscr{S}$ (and hence an inversion of the helicity) can also be achieved by exchanging the *momentum directions* $\hat{\boldsymbol{k}}_a, \hat{\boldsymbol{k}}_b$. On the other hand, the Pauli principle imposes the condition that for a given helicity state of the photon, the coincidence rate should be invariant under an exchange of the roles of the two emerging *electrons*, as stated in Eq. (3.16). Thus, it is useful to look into the role of the Pauli principle and its effect on the CD. For this we choose a situation where the photon beam is perpendicular to the plane spanned by $\hat{\boldsymbol{k}}_a, \hat{\boldsymbol{k}}_b$. The coincidence rate depends only on the electrons' energies and the inter-electronic angle θ_{ab}. Therefore, we choose, without any loss of generality, the x-axis as the bisector of θ_{ab} (cf. Fig. 1). In Fig. 1(a) and Fig. 1(b) we consider the same experimental set-up with, respectively, positive and negative helicity of the photon. Thus the CD is the different in the coincidence rate between the situation in Fig. 1(a) and Fig. 1(b). It is clear that Fig. 1(a) cannot be obtained from Fig. 1(b) by any rotation operation. The Pauli-principle requires that the outcome of the experiment should be the same for cases of Fig. 1(a) and Fig. 1(d). Equivalently, the set-up of Figs. 1(b) and (e) should yield the same results. It is clear from the diagrams that the fast electron (indicated by the longer arrow) is situated always to the right of the x-axis and this situation

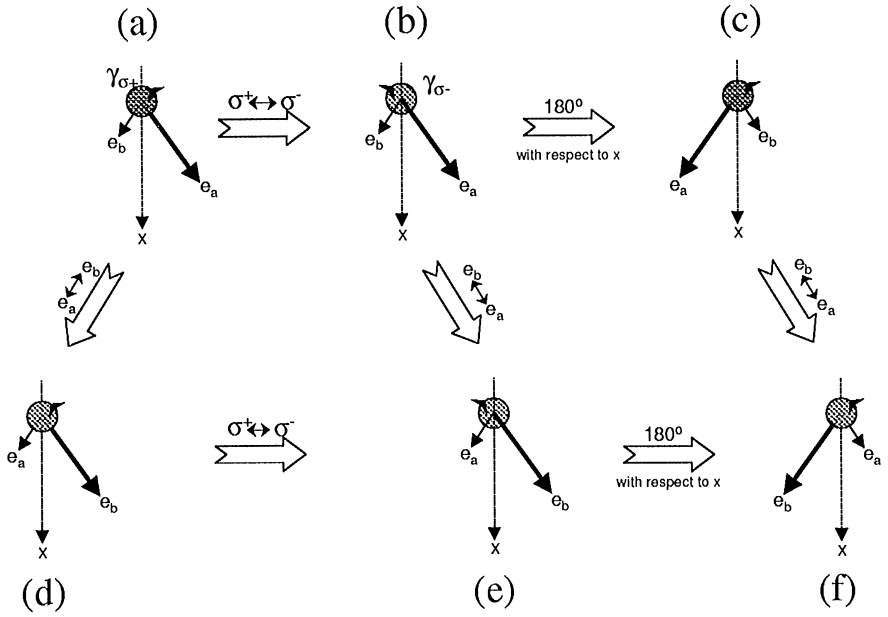

Fig. 1. An illustration of the role of the Pauli principle in the chiral electron-pair emission following the absorption of a single photon. The wave vector of the photon is perpendicular to the plane of the drawing and its helicity is indicated by $\gamma_{\sigma\pm}$. The x-axis is the bisector of the inter-electron emission angle. The arrows labelled by e_a and e_b indicate the emission direction of the photoelectrons and their lengths correspond to their relative energies.

remains unchanged upon inclusion of the Pauli principle. As shown in Fig. 1(b) and Fig. 1(c) as well as in Fig. 1(e) and Fig. 1(f), the helicity state can be flipped from σ^- to σ^+ by a 180° rotation at the x-axis. However, in this case the faster electron will emerge left to the x-axis. From these diagrams (cf. in particular Fig. 1(b) and Fig. 1(c)) it is obvious that the CD disappears when the two electrons escape with equal energies and/or they emerge parallel or anti-parallel to each others. In this sense the CD can be regarded as a left–right asymmetry effect. The appearance of this asymmetry is a manifestation of the parity conservation: The system as a whole (the photon and the atom) has a certain parity, carried in the initial state by the photon. After the photon had been absorbed, this parity state is given over to the two electrons that become a chiral electron pair.

3.5. Consistency conditions

Having established the general features of the CD we turn now to the actual calculations of its value for various kinematics and targets. Before introducing sophisticated dynamical models it is instructive to develop consistency checks that are independent of the specific theoretical or experimental approach. To this end we construct the circular polarised state of the photons from two independent linear polarised states. Using a co-ordinate system where the z-axis is aligned along the wave vector of the circular photon, the optical transition amplitude with left (right)-hand circularly polarised light, labelled as T_{σ^+} (T_{σ^-}), can thus be written as

$$T_{\sigma^\pm} = c(T_x \pm \mathrm{i}T_y)\,. \tag{3.30}$$

Here, T_x (T_y) is the transition amplitude for the DPE with linear polarised light where the electric field vector is aligned along the x (y) direction, and $c = 1/\sqrt{2}$. The photoelectrons are emitted with momenta $\boldsymbol{k}_a$ and $\boldsymbol{k}_b$ determined in the co-ordinate system x, y, z. For the following it is instructive to write Eq. (3.30) in the form

$$T_{\sigma^\pm} = c[|T_x|\exp(\mathrm{i}\phi_x) + |T_y|\exp(\mathrm{i}\phi_y \pm \mathrm{i}\pi/2)]\,, \tag{3.31}$$

where ϕ_x (ϕ_y) is the phase of T_x (T_y). Thus, the quantities $|T_{\sigma^\pm}|^2$ that determine the cross-section (3.1) attain the form

$$|T_{\sigma^\pm}|^2 = \tfrac{1}{2}[|T_x|^2 + |T_y|^2 \pm 2|T_x||T_y|\sin(\phi_y - \phi_x)]\,. \tag{3.32}$$

For the following, it is useful to define a normalised CD as CD_n such that

$$\mathrm{CD}_n := \frac{\mathrm{CD}}{W(\sigma^+, \boldsymbol{k}_a, \boldsymbol{k}_b) + W(\sigma^-, \boldsymbol{k}_a, \boldsymbol{k}_b)}\,. \tag{3.33}$$

From Eq. (3.32) we obtain

$$\mathrm{CD}_n = \frac{2|T_x||T_y|}{|T_x|^2 + |T_y|^2}\sin(\phi_y - \phi_x)\,. \tag{3.34}$$

Equivalently, one can show that

$$\mathrm{CD}_n = -\frac{2}{|T_x|^2 + |T_y|^2}\,\mathrm{Im}(T_y T_x^*)\,. \tag{3.35}$$

In line with the preceding sections we conclude therefore that by changing the polarisation state of the photon information on the *phase differences* of the optical transition amplitudes can be obtained. A quantity that is independent of the polarisation state of the photon can be deduced from $|T_x|^2$ and $|T_y|^2$ to be

$$\Sigma := |T_{\sigma^+}|^2 + |T_{\sigma^-}|^2 = |T_x|^2 + |T_y|^2 \ . \tag{3.36}$$

In addition to this polarisation independent quantity, we can characterise the dependence of the PDI process with linear polarised light on the direction of the polarisation *axis* by defining a normalised *linear dichroism* (LD_n) as

$$\mathrm{LD}_n = \frac{|T_x|^2 - |T_y|^2}{\Sigma} \ . \tag{3.37}$$

We remark however, that $|T_x|^2$ and $|T_y|^2$ differ only in the orientation of the reference axis defined by the oscillating electronic field vector of the photon. Therefore, the LD_n does not provide further dynamical details (such as the phase information) other than those already contained in $|T_x|^2$ and $|T_y|^2$.

The polarisation-independent relation (3.36) does not rely on a specific theoretical model for the absorption dynamics (except for the dipole approximation for the radiation field). Thus, Eq. (3.36) is in sofar useful as it can be used to check the consistency of the cross-sections $|T_{\sigma^\pm}|^2$ with $|T_{x/y}|^2$ (calculated or measured), as done in Ref. [45]. In addition, we can use Eq. (3.36) to test the consistency of PDI cross-sections with linear polarised light, i.e. the internal consistency of $|T_x|$ and $|T_y|$. To see this let us consider the situation where both electrons are detected in the x–y plane. In this case one can show that

$$T_{\sigma^\pm}(\varphi_a - \varphi_b) = T_{\sigma^\pm}(\varphi'_a - \varphi'_b), \quad \{\forall \varphi'_a, \varphi'_b, \varphi_a, \varphi_b \in [0, 2\pi] \,|\, \varphi_a - \varphi_b = \varphi'_a - \varphi'_b\} \ .$$

This means, $T_{\sigma^\pm}$ depend on the inter-electronic relative angle only. Therefore, according to Eq. (3.36), the following equality applies:

$$\begin{aligned} \Sigma(\varphi_a - \varphi_b) = \Sigma(\varphi'_a - \varphi'_b) &= |T_x(\varphi_a - \varphi_b)|^2 + |T_y(\varphi_a - \varphi_b)|^2 \\ &= |T_x(\varphi'_a - \varphi'_b)|^2 + |T_y(\varphi'_a - \varphi'_b)|^2 \ . \end{aligned} \tag{3.38}$$

We note on the other hand that

$$T_{x/y}(\varphi_a - \varphi_b) \neq T_{x/y}(\varphi'_a - \varphi'_b) \quad \text{for } \varphi_{a/b} \neq \varphi'_{a/b} \ .$$

Hence, the inter-relation Eq. (3.38) for the PDI measurement with linear polarised light must be given.

From Eq. (3.34) it is readily deduced that

(a) the CD vanishes for $\phi_y - \phi_x = n\pi$ and n is an integer, this is for example the case where T_y and T_x are both pure imaginary or pure real. We remark here, that the phases depend on the frequency in a dynamical way. Thus, it might well be that at a certain frequency the phase relation is such that the CD_n vanishes (see the calculations below).

(b) The CD_n vanishes when T_x and/or T_y vanishes. This observation is most valuable for interpreting the structure of the measured cross-sections with polarised light, as done below.

(c) The CD_n diminishes as $|T_l|/|T_j|$; $j = x, y$; $l = y, x$ for $|T_j| \gg |T_l|$. This condition can be used to reveal the high- and low-frequency behaviour of the PDI cross-section [45].

3.6. Closed analytical expressions for the circular dichroism

The previous sections revealed a wealth of information about the properties of the circular dichroism and the information contained within. However, we were basically able to make some predictions concerning the geometry where the dichroism vanishes. It is clear that if the CD is to be finite there must be kind of a peak or probably structured peak between the various situations where the dichroism diminishes. For an accurate prediction of the size and shape of the CD one has to resort to some modelling of the many-body states (at least two electrons in the field of a positive point charge). Before presenting sophisticated theories that cannot give a closed analytical formula for the CD we investigate simpler cases in which the rough behaviour and size of the CD can be deduced analytically. As it is clear from Eq. (3.1), expressions for the many-body wave functions in the initial ($|\Phi_i\rangle$) and the final state ($|\Psi^-\rangle$) are needed. While, the initial bound state can be described theoretically with standard methods to a very good accuracy, the correlated dynamics in the final state is still a challenge for theorists. Here we have to resort to simple expressions for $|\Phi_i\rangle$ and $|\Psi^-\rangle$ to arrive at analytical results for the CD. For an initial two-electron state with $^1S^e$ symmetry we employ the expression

$$\Phi_s = N_s \exp[-Z_s(r_a + r_b)] , \tag{3.39}$$

where $\boldsymbol{r}_a$ and $\boldsymbol{r}_b$ are the positions of the two electrons with respect to the nucleus. The parameter Z_s is variationally determined by minimising the binding energy and N_s is a normalisation factor. A Ritz variational procedure [81] yields $Z_s = Z - 5/16$, $N_s = Z_s^3/\pi$, where Z is the nuclear charge. This means by using (3.39) we account for the electron–electron interaction as a mere effective (angular and radially independent) screening of the nuclear interaction. According to (3.39), in the limit of $Z \gg 1$ we obtain $Z_s \approx Z$, i.e. the electron–electron interaction can be neglected altogether in favour of the nuclear one. In the final state we assume the two electrons to move in an effective field of the nucleus. The electron–electron interaction is subsumed into a dynamical screening of the strength of interaction of the electrons with the residual ion. Mathematically formulated this yields for $|\Psi^-\rangle$ the expression [81]

$$\begin{aligned}\Psi^-_{\boldsymbol{k}_a,\boldsymbol{k}_b}(\boldsymbol{r}_a,\boldsymbol{r}_b) \approx \Psi_{2c} := (2\pi)^{-3} N_a N_b \mathrm{e}^{\mathrm{i}\boldsymbol{k}_a\cdot\boldsymbol{r}_a + \mathrm{i}\boldsymbol{k}_b\cdot\boldsymbol{r}_b}\, {}_1F_1[\mathrm{i}\beta_a, 1, -\mathrm{i}(k_a r_a + \boldsymbol{k}_a\cdot\boldsymbol{r}_a)] \\ {}_1F_1[\mathrm{i}\beta_b, 1, -\mathrm{i}(k_b r_b + \boldsymbol{k}_b\cdot\boldsymbol{r}_b)] .\end{aligned} \tag{3.40}$$

Here, the functions ${}_1F_1(a,b,z)$ are the confluent hypergeometric functions [75] and the Sommerfeld parameters, that characterise the strength of the two-particle Coulomb interaction, are given by $\beta_{a/b} := -Z_{a/b}/k_{a/b}$. There are various models for deriving reasonable values of the effective charges ([76] and references therein). It is not our purpose here to go into the details of this subject. For the sake of simplicity and clarity we make the replacement $Z_a = Z = Z_b$, i.e. we neglect screening effects. The same mathematical steps involved in the derivation of the CD can be repeated when $Z_{a/b}$ depend on the momenta of the two electrons. The normalisation constants in Eq. (3.40) N_j, $j = a, b$ are given by $N_j = \exp(-\pi\beta_j/2)\Gamma(1 - \mathrm{i}\beta_j)$, $j = a, b$. Upon the replacement

$\beta_a \equiv 0 \equiv \beta_b$ in Eq. (3.40) we arrive at the plane wave approximation for the photoelectrons and the optical transition amplitude in velocity form derives from the expression

$$\langle \boldsymbol{k}_a, \boldsymbol{k}_b | \hat{\varepsilon} \cdot (\nabla_a + \nabla_b) | \Phi_i \rangle = \int \mathrm{d}\boldsymbol{p}\, \mathrm{d}\boldsymbol{q} \langle \boldsymbol{k}_a, \boldsymbol{k}_b | \hat{\varepsilon} \cdot (\nabla_a + \nabla_b) | \boldsymbol{p}, \boldsymbol{q} \rangle \langle \boldsymbol{p}, \boldsymbol{q} | \Phi_i \rangle$$

$$= \mathrm{i}\hat{\varepsilon} \cdot (\boldsymbol{k}_a + \boldsymbol{k}_b) \tilde{\Phi}_i(\boldsymbol{k}_a, \boldsymbol{k}_b) \,, \tag{3.41}$$

where $|\boldsymbol{p}, \boldsymbol{q}\rangle$ is a complete set of plane waves and $\tilde{\Phi}_i(\boldsymbol{k}_a, \boldsymbol{k}_b)$ is the (six-dimensional) Fourier transform of the initial state. Since the initial state is randomly oriented the Fourier transform is real and the expression (3.41) is imaginary for any real polarisation vector. Thus, according to Eq. (3.35), the CD vanishes in the plane-wave approximation. Eq. (3.41) makes clear that the phases ϕ_x and ϕ_y are primarily related to the functional dependence of the phases of the final state, for Eq. (3.41) is valid for the exact final-state wave function if rewritten in the form

$$\langle \Psi^-_{\boldsymbol{k}_a, \boldsymbol{k}_b} | \hat{\varepsilon} \cdot (\nabla_a + \nabla_b) | \Phi_i \rangle = \mathrm{i}\hat{\varepsilon} \cdot \int \mathrm{d}\boldsymbol{p}\, \mathrm{d}\boldsymbol{q} (\boldsymbol{p} + \boldsymbol{q}) \tilde{\Psi}^{-*}_{\boldsymbol{k}_a, \boldsymbol{k}_b}(\boldsymbol{p}, \boldsymbol{q}) \tilde{\Phi}_i(\boldsymbol{p}, \boldsymbol{q}) \,. \tag{3.42}$$

Again, the random initial state does not contribute to the phase accumulation (as described by the integral) to result in the dynamical phases ϕ_x and ϕ_y. In Eq. (3.42) $\tilde{\Psi}^-_{\boldsymbol{k}_a, \boldsymbol{k}_b}$ is the Fourier transform of the two-electron final state whose phase is the decisive quantity for the CD. This makes comprehensible why the s^2 configuration in the final state cannot contribute to the dichroism whereas the simplest approximation of the final state as being (s, p) $^1P^o$ leads to a finite dichroism [37].

Using expressions (3.40) and (3.39), the dichroism, $\mathrm{CD}(\boldsymbol{k}_a, \boldsymbol{k}_b)$, is calculated in closed form (see Appendix A):

$$\mathrm{CD} = -ZF(k_a - k_b)(\hat{\boldsymbol{k}}_a \times \hat{\boldsymbol{k}}_b) \cdot \hat{\boldsymbol{k}} \,. \tag{3.43}$$

The function F reads

$$F(k_a, k_b) = 2C_a(Z_s - Z)^2(2Z_s - Z)^2(2f_a f_b)^2(k_a^2 + Z_s^2)^{-5}(k_b^2 + Z_s^2)^{-5} \,, \tag{3.44}$$

where C_a and f_j, $j = a, b$ are given by Eqs. (A.4) and (A.7), respectively. Again we recover, the geometric and energetic symmetry properties of CD, as respectively given by the triple vectorial product and the factor $(k_a - k_b)$. The function F contains further dynamical information. Since $(k_a - k_b)$ and $(\hat{\boldsymbol{k}}_a \times \hat{\boldsymbol{k}}_b) \cdot \hat{\boldsymbol{k}}$ are both antisymmetric with respect to exchange of the two electrons, we deduce $F(k_a, k_b) = F(k_b, k_a)$, for Eq. (3.35) must be satisfied. Furthermore, upon inspection of $F(k_a, k_b)$ (Eq. (3.44)) we verify that F is positive definite for all combinations of $\boldsymbol{k}_a$ and $\boldsymbol{k}_b$. This means that, within the approximations (3.39) and (3.40), CD does not vanish except for the zero points of $(k_a - k_b)(\hat{\boldsymbol{k}}_a \times \hat{\boldsymbol{k}}_b) \cdot \hat{\boldsymbol{k}}$. This conclusion is also valid for the normalised dichroism CD_n, as defined by Eq. (3.33), since F/Σ ($\Sigma := W(\sigma^+) + W(\sigma^-)$) is also positive definite ($\Sigma > 0$). These statements concerning the CD_n apply for all wave functions that contain the inter-electronic interaction via a co-ordinate-independent multiplicative factor [44], since this factor will cancel out when taking the ratio CD/Σ.

Therefore, we conclude, that a vanishing CD at situations other than those dictated by $(k_a - k_b)(\hat{\boldsymbol{k}}_a \times \hat{\boldsymbol{k}}_b) \cdot \hat{\boldsymbol{k}}$ are traced back to effects of the electron–electron interaction other than the static screening of the residual-ion field.

3.7. Dependence of the circular dichroism on the strength of the residual ion's field

As remarked previously the approximate forms (3.40) and (3.39) become more appropriate with increasing nuclear charge Z. Therefore, it is worthwhile to study the CD using Eqs. (3.40) and (3.39) for moderately large Z (we still neglect however the $\boldsymbol{L}\cdot\boldsymbol{S}$ interaction, i.e. Z should not be too large for the $\boldsymbol{L}\cdot\boldsymbol{S}$ to become sizeable). Generally, with increasing Z the photodouble-ionisation cross-section decreases rapidly; in contrast the CD_n remains finite. This follows from the expression for CD_n,

$$\mathrm{CD}_n = -\frac{Z}{\mathscr{F}}(k_a - k_b)(\hat{\boldsymbol{k}}_a \times \hat{\boldsymbol{k}}_b)\cdot\hat{\boldsymbol{k}}\ , \tag{3.45}$$

where $\mathscr{F} = \Sigma/F$ is given by Eq. (A.18). As Σ and F are positive-definite functions of k_a and k_b, we conclude $\mathscr{F}(k_a, k_b) > 0$. For the case that the photon beam is perpendicular to the plane spanned by $\hat{\boldsymbol{k}}_a$ and $\hat{\boldsymbol{k}}_b$, the function $\mathscr{F}$ simplifies to

$$\mathscr{F} = \frac{k_b^2 + Z_s^2}{k_a^2 + Z_s^2}(k_a^2 + Z^2) + \frac{k_a^2 + Z_s^2}{k_b^2 + Z_s^2}(k_b^2 + Z^2) + 2(k_a k_b + Z^2)\cos\theta_{ab}\ . \tag{3.46}$$

The behaviour of CD_n as function of Z is pretty much dependent on the experimental situation. For example, if we consider the CD_n as function of θ_{ab} for energies of the electrons such that $k_a \gg Z \ll k_b$, then the Z dependence of $\mathscr{F}$ can be neglected and the CD_n increases with increasing Z. For very asymmetric energy sharing, however, the function $\mathscr{F}$ [Eq. (3.46)] becomes proportional to Z^2 for large nuclear charge. Therefore the CD_n decreases with increasing Z. The latter behaviour can be seen in Fig. 2 for $\mathrm{Li}^+(^1S^e)$, $\mathrm{Be}^{2+}(^1S^e)$ and $\mathrm{B}^{3+}(^1S^e)$ as targets. From Fig. 2 it is also clear that the CD_n is less sensitive to changes in the ionisation dynamics than the cross-sections. Unfortunately, there is as yet no experimental data for the CD_n for a varying residual ion charge.

3.8. The photon-frequency dependence

The photon-frequency dependence of the CD_n close to the double ionisation threshold can be investigated within the Wannier–Peterkop–Rau (WPR) theory that has been discussed in Section (3.3). As well known the gerade and the ungerade amplitudes a_g and a_u obey different threshold laws, namely

$$|a_\mathrm{g}|^2 \propto E^{n-2}\ ,$$

$$|a_\mathrm{u}|^2 \propto E^{3n-3/2}\ ,$$

where $E = E_a + E_b$ is the total excess energy and n is the Wannier exponent [71] (its numerical value is, e.g. $n = 1.127$ for H^- and $n = 1.056$ for He). For small E, the *gerade* amplitude a_g dominates over the *ungerade* amplitude a_u within a small energy range of unknown extension. The dichroism being proportional to the *interference* between a_g and a_u possesses the energy dependence

$$\mathrm{CD} \propto E^{2n-7/4}\sin\theta_a \sin\theta_b \sin\varphi\ . \tag{3.47}$$

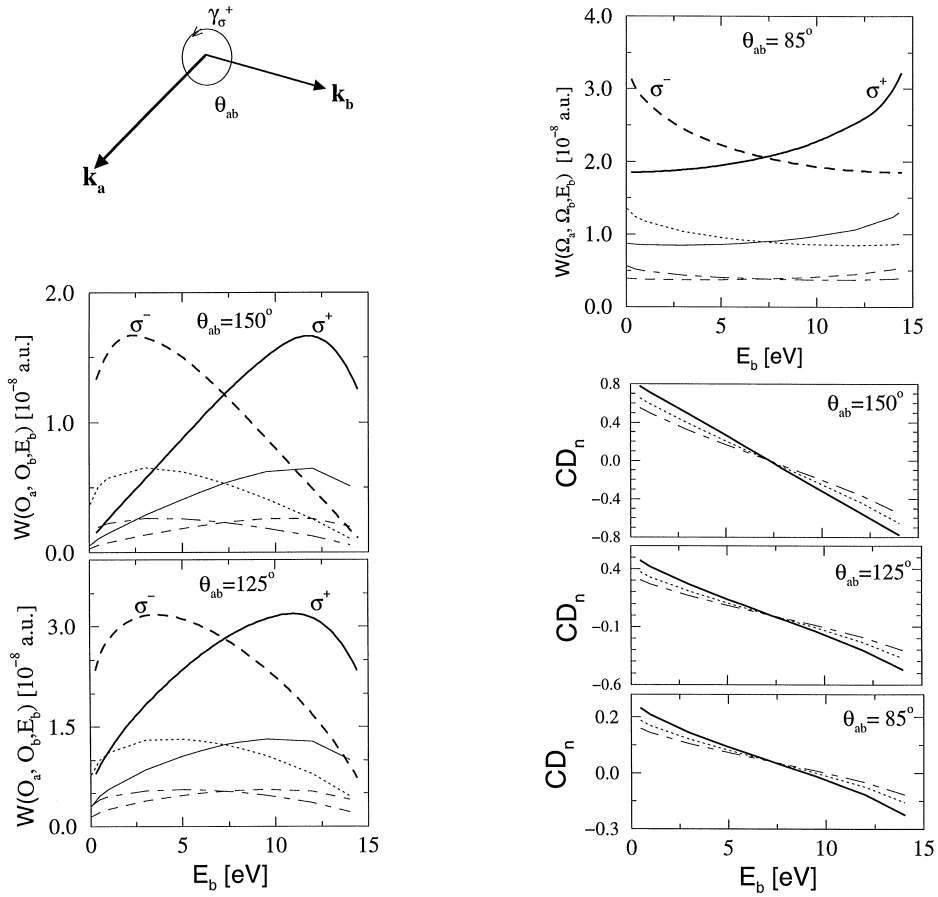

Fig. 2. The one-photon double ionisation of $Li^+(^1S^e)$, $Be^{2+}(^1S^e)$, $B^{3+}(^1S^e)$. As sketched, the two electrons escape in the plane of the drawing that is perpendicular to the photon beam. For a fixed relative angle between the electrons θ_{ab}, the energy of one the electrons, say E_b, is varied while the the excess energy $E = E_a + E_b$ is fixed to be 14.5 eV [$E_a = 14.5 - E_b$ (eV)]. The photon energy is varied as to compensate for the different double-ionisation potentials of the different targets. The figures show: $W(Li^+, \sigma^+)$: thick solid curve, $W(Li^+, \sigma^-)$: thick dashed curve, $W(Be^{2+}, \sigma^+)$: solid thin curve, $W(Be^{2+}, \sigma^-)$: dotted curve, $W(B^{3+}, \sigma^+)$: dashed thin curve, and $W(B^{3+}, \sigma^-)$: dash-dotted curve. Also shown is the dichroism CD_n for the case of Li^+ (solid curve), Be^{2+} (dotted curve), and B^{3+} (dash-dotted curve). The cross-section for Be^{2+} (B^{3+}) has been multiplied by a factor of 2 (3). For the calculations we employed the analytical formulas, as given by Eqs. (3.40) and (3.39).

A finite dichroism close to threshold is not forbidden by this consideration but approaching threshold we expect a decreasing dichroism as predicted by (3.47). The range of validity of this law is closely related to that of the WPR theory. When compared with the measured *total* photo-double-ionisation cross-sections [82] the WPR theory provides reliable predictions within 2 eV above threshold. It should be stressed however, that the CD is essentially a differential quantity (it vanishes when integrated over one of the electrons) whereas the WPR is designed for integrated cross-sections. The predictions of the WPR theory for the frequency dependence of CD and of CD_n (near threshold the behaviour of $\Sigma(E)$ is determined by $|a_g|^2$) can now be compared with the

analytical results of Section 3.6. To do this we note that the photon-frequency dependence of Σ and CD_n, as described by Eqs. (A.16) and (3.45), is more transparent in the parameterisation $k_a = \sqrt{2E}\sin\alpha$, $k_b = \sqrt{2E}\cos\alpha$ (E is the excess energy). Eq. (3.45) reads then, $CD_n = Z\sqrt{2E}(\cos\alpha - \sin\alpha)(\hat{\boldsymbol{k}}_a \times \hat{\boldsymbol{k}}_b)\cdot\hat{\boldsymbol{k}}/\mathscr{F}$, where

$$\mathscr{F} = \frac{2E\cos^2\alpha + Z_s^2}{2E\sin^2\alpha + Z_s^2}(2E\sin^2\alpha + Z^2) + \frac{2E\sin^2\alpha + Z_s^2}{2E\cos^2\alpha + Z_s^2}(2E\cos^2\alpha + Z^2) + 2E(\sin 2\alpha + Z^2)\cos\theta_{ab} \ .$$

Since $\mathscr{F} = F/\Sigma$ and the function $F(E)$, as given by Eq. (A.12), is positive definite it follows that $\mathscr{F}(E)$ is positive definite as well. At threshold ($E \to 0$) the CD_n decreases as $\sqrt{E}$. For high photon frequency ($E \to \infty$) the CD_n is proportional to $1/\sqrt{E}$. Except for these two limits the CD_n possesses no additional zero points as function of E (this is due to $\mathscr{F}(E) > 0$, $\forall E$ and $CD_n \propto \sqrt{E}/\mathscr{F}$). These conclusions are applicable when employing the approximate wave functions (3.40) and (3.39). Any additional zero points in the CD_n as function of E has to be assigned to the electron–electron interaction in the initial and/or final state, as discussed later on.

3.9. Calculational schemes of the polarised one-photon two-electron transitions

In Section 3.6, we were able to derive analytical results for the dichroism and the cross-sections. From the structure of the wave functions (3.40) it is clear however that the double-ionisation dynamics is probably oversimplified, at least for cases with strong electronic correlation. More accurate results are provided by including the electron–electron interaction either analytically, as in the three-body Coulomb wave model (3C), or full numerically, as in the convergent close coupling method (CCC). It should be noted here that there is a considerable body of theoretical treatment of the one-photon double ionisation by linear polarised photon which have been summarised recently in Ref. [54]. Here we focus on those models that have been employed for the evaluation of the dichroic effects in double photoionisation.

In the 3C treatment Eq. (3.40) is extended to include the final-state electron–electron interaction in the form (cf. Refs. [76–79])

$$\Psi_{3C} = N_{ab}\Psi_{2c} \ {}_1F_1[i\beta_{ab}, 1, -i(k_{ab}r_{ab} + \boldsymbol{k}_{ab}\cdot\boldsymbol{r}_{ab})] \ , \tag{3.48}$$

where $\boldsymbol{r}_{ab} := \boldsymbol{r}_a - \boldsymbol{r}_b$ and $\boldsymbol{k}_{ab}$ is its conjugate momentum, $\beta_{ab} := 1/2k_{ab}$ and $N_{ab} = \exp(-\pi\beta_{ab}/2)\Gamma(1 - i\beta_{ab})$. In what follows we improve on the description of the initial state by employing a correlated Hylleraas initial state

$$\Phi_{3h} = N_h[\exp(-\alpha_{h1}r_a - \alpha_{h2}r_b) + \exp(-\alpha_{h1}r_b - \alpha_{h2}r_a)]\exp(\beta r_{ab}) \ . \tag{3.49}$$

The parameters $\alpha_{h1/h2}, \beta$ are variationally determined by minimising the binding energy.

It is out of the scope of this work to go into the very details of the approximate wave functions (3.48) and (3.49), the interested reader can find comprehensive details in Refs. [76–79]. As shown in Ref. [76], when expressed in appropriate co-ordinates, the three-body Hamiltonian (two continuum electrons in the field of a residual ion) can be written as a sum of three two-body Hamiltonians that commute with each other. This means that the three-body system is considered

as a sum of three two-body systems. Thus, in the appropriate non-orthogonal six-dimensional space, the coupling between these individual subsystems is not accounted for by (3.48). This coupling can be incorporated approximately into the theory, but on the considerable expense of introducing a radial dependence of the two-body interaction strength Ref. [76]. This makes the numerical implementation quite involved. In addition, it has not yet been possible to find a method to normalise the coupled three-body wave function in a mathematically sound way. Nevertheless, there are already some numerical implementations of this radially coupled three-body wave function for the double photoionisation, but in view of the above statements concerning the normalisation, these numerical methods and their results are not conceivably conclusive. Nonetheless, we stress here that analytical methods can only be approximate, for the many-problem is not separable. Their role is to serve as a tool to understand the underlying physics, rather than to compete in accuracy with full numerical methods, such as those outlined below.

To get an insight into the effect of the electronic correlation on the chiral electron-pair emission we consider in Fig. 3 the same case studied in Fig. 2 using the wave functions (3.48) and (3.49). Comparing Figs. 2 and 3 we observe that the effect of the electron–electron interaction is less pronounced when the two electrons escape in almost opposite directions ($\theta_{ab} = 150^\circ$). This is

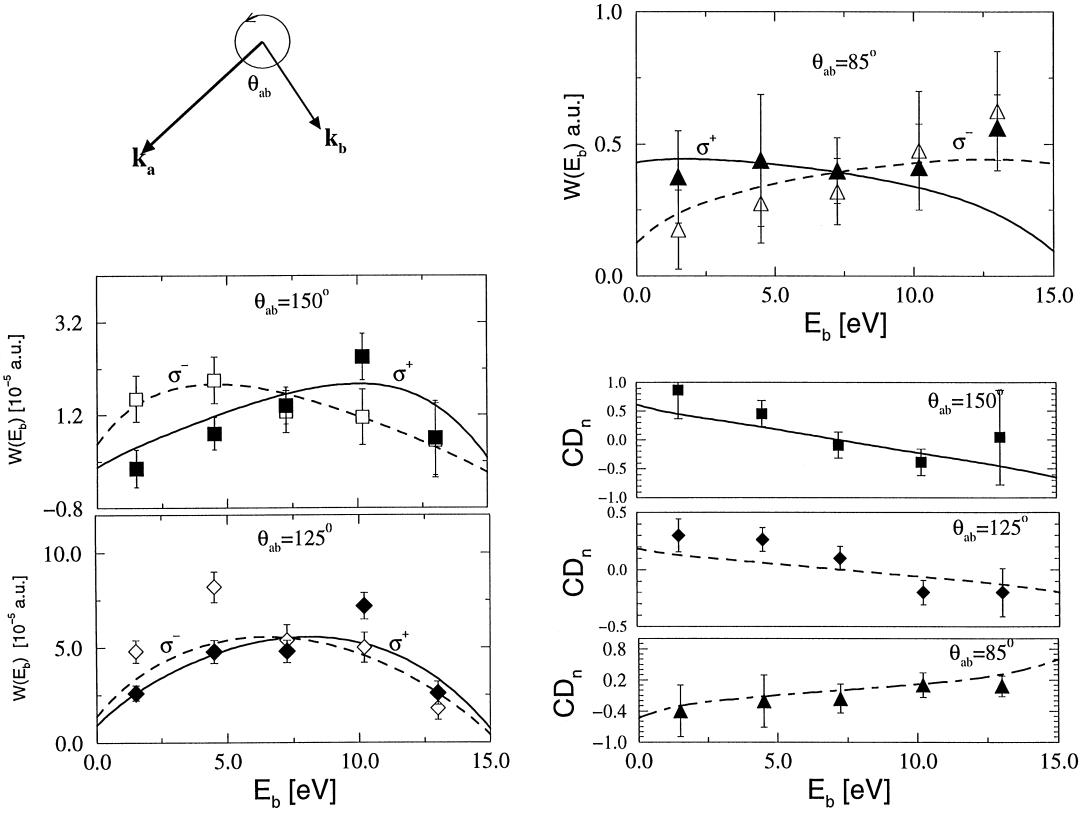

Fig. 3. The same geometry as in Fig. 2 (schematically shown by the drawing), however, the wave function (3.48) has been employed for the final state. The theoretical cross-sections at $\theta_{ab} = 150^\circ$ (85°) have been scaled down by a factor of 2 (3). The target is a helium atom in its ground state. The total energy of the pair is 14.5 eV. Experimental data are due to Ref. [42].

understandable from the properties of the electron–electron repulsion which is strongest when the two electrons escape close to each other. When θ_{ab} becomes smaller the influence of electronic correlation becomes prevalent.

Probably the most notable feature in Fig. 3, as compared to Fig. 2 and to our finding of Section 3.1, is that the CD_n becomes quite small at $\theta_{ab} = 125^\circ$ and changes sign when varying the mutual angle further to $\theta_{ab} = 85^\circ$. This behaviour, which is confirmed by the experimental finding, is in so far surprising as it cannot be explained by the analytical results deduced from the approximation (3.40) and (3.39) nor by the general tensorial analysis of Section 3.1. Since this behaviour of the CD_n occurs only when correlated states are used, we assign it to the electron–electron coupling. However, the underlying physics for this new feature is not clear, i.e. it is still an open question why the phase of the correlated final state wave function behaves such that the phase difference between T_x and T_y vanishes.

For the explanation of the evolution of the size of the CD_n as revealed by Fig. 3 we refer to Ref. [44].

In Figs. 2 and 3 we analysed the energy-sharing behaviour of the CD_n. The angular correlation of the CD_n is investigated in Fig. 4. Since the behaviour of the double ionisation cross-section by linearly polarised photon is well investigated, both theoretically and experimentally, it is appropriate to use Eq. (3.32) to understand the behaviour of the PDI cross-section with polarised photons in light of the behaviour of T_x and T_y. An example is shown in Fig. 4 where calculations and experiment for the PDI cross-sections derived from T_x and T_y are shown. The *shape* of the experimental findings for $|T_x|^2$ and $|T_y|^2$, as shown in Fig. 4(a) is reasonably reproduced by the theory, however, considerable deviations between theory and experiment are observed as far as the magnitude of the cross-sections is concerned. At $\varphi_a = 0, \pi, 2\pi$ the amplitude T_y possesses a zero point since in this case the two photoelectrons escape perpendicular to the linear polarisation vector [80]. We note here, that in general, a *shape* agreement between theory and experiment, as far as $|T_x|^2$ and $|T_y|^2$ are concerned, does not mean the same kind of agreement for the sum Σ of $|T_x|^2$ and $|T_y|^2$ (unpolarised cross-section) [Fig. 4(c)], because the shape of Σ depends on the relative ratio between $|T_x|^2$ and $|T_y|^2$.

Comparing Figs. 4(a), (b) $[|T_{x/y}|^2]$ and (c) (Σ) it is evident that the minimum in Σ at $\varphi_a = \pi$ is due to the zero point in T_y at the same position whereas the two peaks originate from the corresponding peaks in $|T_y|^2$. In fact, the peaks in Σ at $\varphi_a \approx 125^\circ, 235^\circ$ appear as a result of the dip in Σ at $\varphi_a = \pi$.

As it is clear from Eq. (3.32), the difference between Σ, as depicted in Fig. 4(c), and $W(\sigma^\pm)$ depend very much on whether T_x and T_y interfere constructively or destructively. This interference is controlled by the phase difference $\phi_{yx} := \phi_y - \phi_x$. As seen in Fig. 4(d), ϕ_{yx} remains almost unchanged when using different initial-state descriptions, in contrast to Σ [cf. Fig. 4(c)]. From Fig. 4(d) we also notice that when both electrons emerge approximately in the same direction (i.e. in the region $260^\circ < \varphi_a < 100^\circ$), the phase difference ϕ_{yx} is relatively small and smooth. As a result, the cross-sections $W(\sigma^\pm)$ [see Fig. 4(e)] are basically dictated by Σ (which is helicity independent) and consequently do not differ much from each other. On the other hand, when the photoelectrons escape almost opposite to each other ($\varphi_a \approx 180^\circ$) we observe a considerable phase difference ϕ_{yx}. As obvious from the sign of ϕ_{yx} this results in a constructive (destructive) interference of T_x and T_y for $\varphi_a < 180^\circ$ ($\varphi_a > 180^\circ$) leading to the shape of $W(\sigma^+)$, as observed in Fig. 4(e). Same consideration applies to $W(\sigma^-)$. Therefore, one can conclude that the structure of the angular

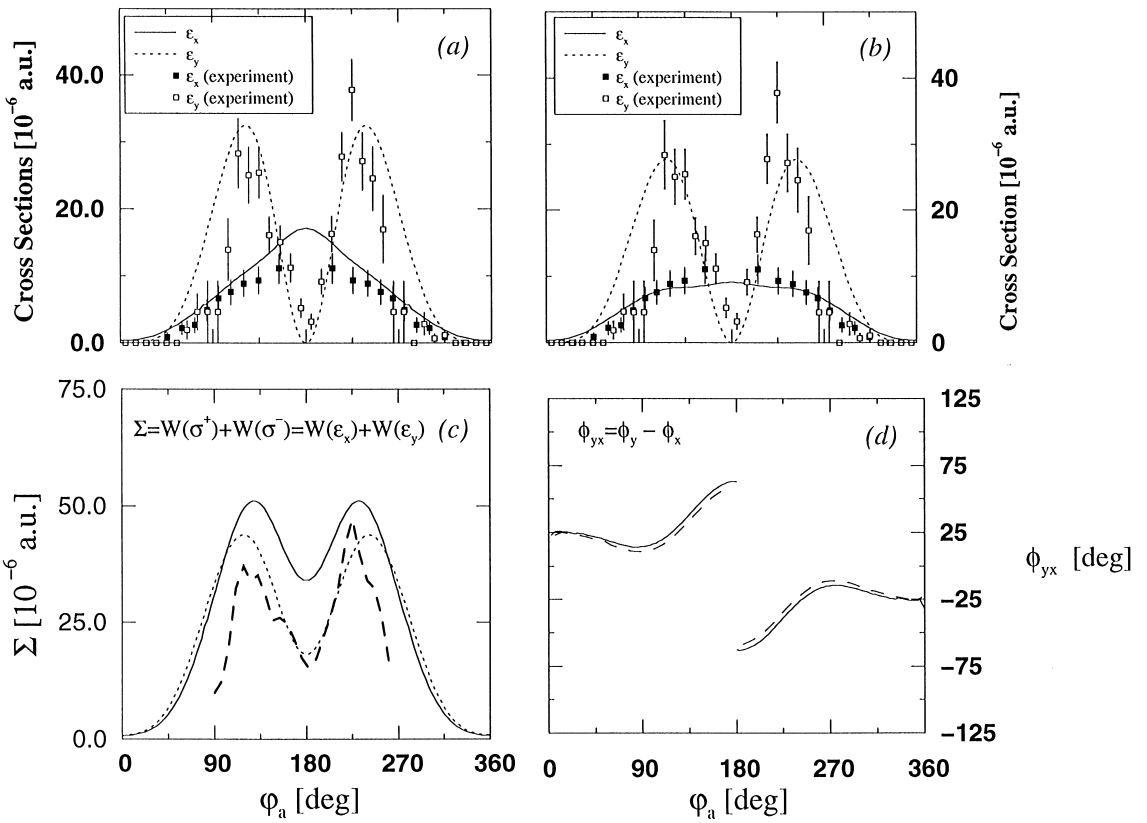

Fig. 4. (a) The cross-sections for the double ionisation of He($^1S^e$) with linear polarised photon. Two cases are depicted where the photon's polarisation vector is fixed along the x- (solid line, labeled ε_x) or the y-direction (dotted curve, labelled ε_y). The excess energy is 20 eV. Both ejected electrons are detected in the x–y plane. One fast electron (electron b with 17.5 eV) is detected along the x-direction whereas the angular distribution of the slower one (electron a) is scanned with φ_a is being its (positive) azimuth angle (with respect to x-axis). Experimental data are provided by Bräuning et al. [83]. In the calculations, the finite energy resolution of $\pm$ 1 eV has not been taken into account. The initial state has been modelled by three-parameters Hylleraas wave function [44,84] whereas the final state is taken as a 3C wave function (see text). Velocity form has been employed. (b) Same geometry and notation as in (a) but the initial state has been modelled by a wave function that partially satisfies the two-body cusp conditions as proposed in Ref. [85]. To allow for shape comparison the solid curves in (a) and (b) have been multiplied by a factor of 2 whereas the dotted curve by a factor of 4. The experimental data are on absolute scale. (c) The sum Σ ($\Sigma = W(\varepsilon_x) + W(\varepsilon_y) = W(\sigma^-) + W(\sigma^+)$) for the detection geometry as in (a). The solid curve has been obtained using the same theoretical model as in (a) whereas the dotted curve derives from the theory of (b). The theoretical results have been multiplied by a factor of 4. The thick dashed curve is the (absolute) experimental Σ as deduced from (a). (d) The difference $\phi_{yx} = \phi_y - \phi_x$ of the phases ϕ_y and ϕ_x of the amplitudes T_y and T_x as used to calculate, respectively, $W(\varepsilon_y)$ and $W(\varepsilon_x)$. The solid (dashed) curve corresponds to the case of (a) [(b)]. (e) The same arrangement of the electrons' detectors, however, the photon is circularly polarised with its wave vector pointing along the z direction. Cross-sections for positive (solid line, labelled σ^+) and negative (dotted line, labelled σ^-) helicity photons are depicted. The calculations are done as in (a) except for the dashed curve where σ^+ has been evaluated using for the initial-state description the wave function proposed in Ref. [85] [same as in (b)]. (f) The circular dichroism CD_n as defined by Eq. (3.7) for the case of (e). The solid curve is the CD_n deduced from the solid and the dotted curves in (e) whereas the dashed curve corresponds to CD_n as predicted by the calculation labelled by the dashed curve in (e). The experimental data are due to Ref. [43].

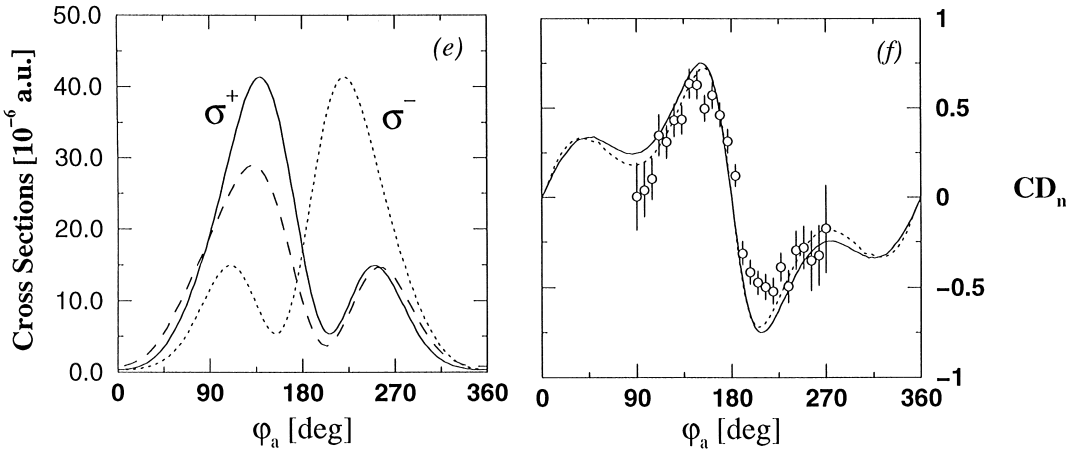

Fig. 4. Continued.

distribution of $W(\sigma^{\pm})$ (two peaks and one minimum) has its origin in the shape of Σ, superimposed on that is the interference pattern of T_x and T_y. In this sense the PDI cross-sections is a more sensitive indicator of the ionisation dynamics than Σ only or CD_n only (of course Σ *and* CD_n are just an exact parameterisation of the cross-sections). In Fig. 4(f) the CD_n is shown along with the experimental data. As expected, the CD_n vanishes at $\varphi_a = 0°, 180°, 360°$. On the other hand, an additional structure appears around $\varphi_a = 90°, 270°$ which is obviously related to the phase properties (cf. Fig. 4(d)) and cannot be explained by geometrical arguments. In fact, this *dynamical minimum* in the CD_n develops to a zero point at certain experimental situation [37].

Fig. 5 demonstrates the element dependence of the PDI cross-section with circularly polarised light as well as the effect of the initial state symmetry. As seen from Figs. 5(a), (b) and (d), the CD_n and the cross-sections depend in an unrelated way on the electronic correlation. To specify completely the PDI process a measurement of both CD_n and Σ are necessary, or equivalenty $W(\sigma^+)$ and $W(\sigma^-)$. The predictions of the wave function (3.40) for the cross-sections are far off those of the correlated one (3.48). In contrast, the predictions for CD_n, as shown in Fig. 5(f), seem to resemble roughly those calculated using Eq. (3.48) [Fig. 5(d)], as far as the shape is concerned.

The PDI cross-section for the triplet state of helium [Fig. 5(c)] is completely different from that for the singlet state [Fig. 5(a)]. A closer look at $|T_x|$ and $|T_y|$ however, reveals that $|T_x|$ and $|T_y|$ obeys now different selection rules and therefore the PDI cross-section for the triplet state shows only one single peak (we recall that the minimum in the PDI cross-section for the singlet state is interpreted as a result of a zero point in $|T_y|$, cf. Fig. 4). On the other hand, the CD in case of triplet has an inverted sign and is much smaller as compared to the case of singlet. The results for CD_n (shown in Fig. 5(f)) indicate that the dichroism for the triplet state is large when the cross-section is small and hence the enhanced value of the CD_n in comparison with the CD_n for the singlet state.

In Fig. 6 we show the angular correlation pattern of the cross-section and of the dichroism when one of angle θ_b between the beam direction and the plane spanned by $\hat{\boldsymbol{k}}_a$ and $\hat{\boldsymbol{k}}_b$ is varied while $\hat{\boldsymbol{k}}_a \perp \hat{\boldsymbol{k}}_b$. As it is clear from Fig. 6 the magnitude of the cross-section does not vary much when θ_b is changed, while CD_n follows the geometric propensity rule of the dichroism.

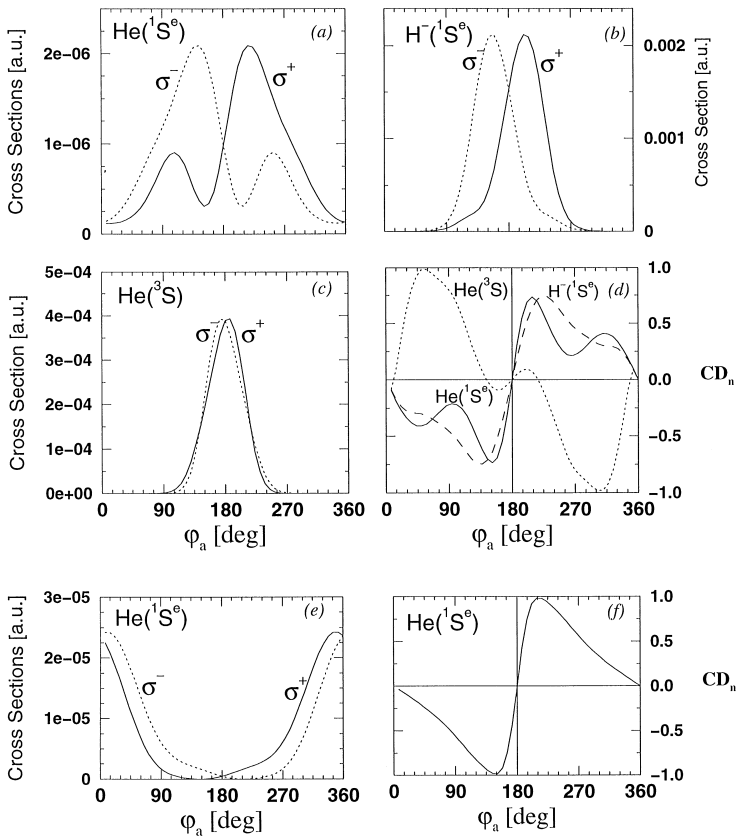

Fig. 5. The same geometry as in Fig. 4(e), however, the energy of the electron fixed along the x-direction is lowered to 1 eV while the energy of the other electron (with variable angle φ_a) is chosen as 12 eV. (a) Shows the cross-section as function of φ_a for He($^1S^e$) whereas in (b) H^-($^1S^e$) is used as a target. In (c) we employ the excited state of helium He(^3S) as an initial state. The photon energy is adjusted as to compensate for the different ionisation potentials of the various targets while keeping fixed the excess energy of the electron pair at 13 eV. In (d) we show CD_n for He($^1S^e$) (solid curve), H^-($^1S^e$) (dashed curve) and He(^3S) (dotted curve). For the calculations shown in (a)–(d) the final state given by Eq. (3.48) has been employed and a three-parameter Hylleraas wave function for the ground state of the target has been used. In (e) and (f) we illustrate the effect of final state interaction by calculating the cross-section (e) and CD_n for the situation corresponding to (a) but using the final-state wave function (3.40) due to which the electron–electron final-state interactions are neglected.

3.10. The convergent close coupling technique

A further powerful numerical method for the calculation of chiral photoelectron pair emission is the *convergent close coupling technique* (CCC). As in the WPR method the absorption of a circularly polarised photon, say by a $^1S^{\text{even}}$ state, leads to a final state with specific magnetic quantum number M. The fully differential cross-section of the PDI process is written as [46,47]

$$W(M,\boldsymbol{k}_a,\boldsymbol{k}_b)=c\left|\sum_{l_a l_b}(-\mathrm{i})^{l_a+l_b}B^{l_a l_b}_{1M}(\hat{\boldsymbol{k}}_a,\hat{\boldsymbol{k}}_b)\mathrm{e}^{\mathrm{i}[\delta_{l_a}(E_a)+\delta_{l_b}(E_b)]}D_{l_a l_b}(E_a,E_b)\right|^2, \tag{3.50}$$

where c is a constant which depends on the normalisation of the continuum wave functions and the gauge of the electromagnetic operator. The index M indicates the polarisation of light and is set to 0 for linearly polarised light and to ± 1 for circularly polarised light depending on the helicity, i.e. $W(M = \pm 1, \boldsymbol{k}_a, \boldsymbol{k}_b) \equiv W(\sigma^{\pm}, \boldsymbol{k}_a, \boldsymbol{k}_b)$. The "quantisation axis" (z) is chosen along the polarisation axis for $M = 0$ whereas for $M = \pm 1$ it is directed along the photon beam propagation.

Expression (3.50) is compatible with the general formalism of Section 3.1. This can be easily seen in the case of a ^1S two-electron initial state in which case Eq. (3.50) can be written as

$$W(M, \boldsymbol{k}_a, \boldsymbol{k}_b) = C \sum_{L} \sum_{L_a L_b} \langle L0 \,|\, 1M, 1 - M \rangle B_{L0}^{L_a L_b}(\hat{\boldsymbol{k}}_a, \hat{\boldsymbol{k}}_b) \gamma_{L_a L_b}(E_a, E_b) \,. \tag{3.51}$$

The dynamical function γ depends on the energies, the angular momentum coefficients, phases and the reduced matrix elements, but has no M-dependence. The dependence on M is included in the Clebsch–Gordan coefficient (the summations over L_a, L_b and $L = 0, 1, 2$ are independent of M). When calculating the CD, only the term $L = 1$ and $L_a = L_b$ terms survive in accord with the derivation of Section 3.1.

For the calculation of the reduced dipole matrix element $D_{l_1 l_2}(E_1, E_2)$ one expands the final two-electron continuum state using N square-integrable (L^2) states, with the double ionisation processes being identified with excitation of the positive-energy pseudostates. Technical details can be found in Refs. [46,47]. Basically, the method treats the double ionisation as a photoionisation with a true continuum electron of energy E_a and orbital angular momentum l_a accompanied with excitation of the ionic electron to a state denoted by $n_b l_b$ with energy E_b. Thus, in a sense, the CCC method employs boundary conditions corresponding to a situation where the true continuum electron always being shielded by the "excited" one, irrespective of the energies E_a and E_b. This seems reasonable for an asymmetric energy sharing $E_a \gg E_b$ but leads to some problems when $E_b \gg E_a$. As discussed in Ref. [86], one can design a strategy to control these problems. There are now a number of application of the CCC method to the case of PDI with linear polarised light. In the context of this work we briefly discuss recent CCC result for the PDI with circular polarised light [46,47].

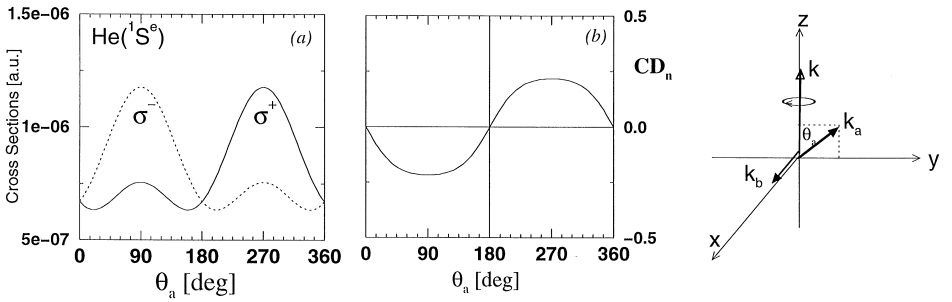

Fig. 6. The variation of the cross-section (a) and CD_n (b) as function of the polar angle θ_a of one of the emitted electrons while the energy and angles of the other electron are fixed. The energies and the target as well as the employed theoretical models are the same as in Fig. 5(a) where θ_a is varied in the x–z plane, i.e. we choose $\varphi_a = 90^\circ$ and $\varphi_b = 0$ (see also the schematic drawing of the process).

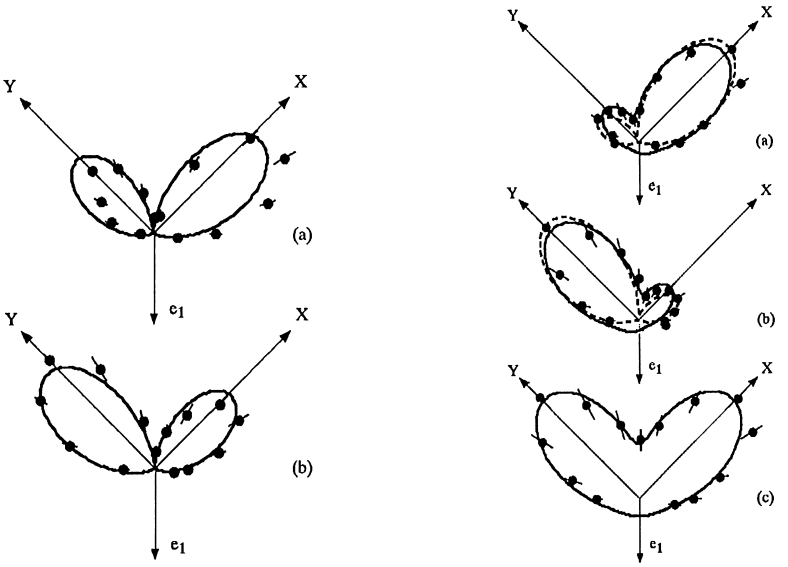

Fig. 7. The angular correlation of the double photoionisation cross-section in the equal energy-sharing mode. Both electrons escape with equal energies $E_a = E_b = 4.5\,\text{eV}$. The Stokes parameters are for inset (a) $S_1 = +0.20$, $S_3 = -0.95$ whereas for inset (b) $S_1 = -0.20$, $S_3 = +0.95$ (cf. Eqs. (3.36) and (3.52)). The emission direction of one electron is fixed at the position labelled by the arrow whereas the angle of emission of the second electron is varied in the plane of the drawing. The experiment (full dots) is shown along with the results of the fitting formula according to Refs. [48,49]. The figures are due to Ref. [50].

Fig. 8. The same as in Fig. 7, however the electron fixed at the position indicated by the arrow escapes with 1 eV energy. The other electron whose emission angle is scanned possesses an energy of 8 eV. According to Eqs. (3.36) and (3.52), the Stokes parameters have to be determined. These are $S_1 = -0.2$, $S_3 = 0.95$ for the case shown in (a) whereas for (b) $S_1 = -0.20, S_3 = +0.95$. Inset (c) shows the sum of the cross-sections depicted in (a) and (b) (cf. Eqs. (3.36) and (3.52)). Experimental data (full dots) are shown along with the result of the fitting procedure of Refs. [48,49] (solid curve) whereas the dashed curves are the results of the CCC theory [47,46,88]. Both the experiment and theory are arbitrarily scaled for comparison. The results are due to Ref. [50].

Before we discuss the CCC data as compared to recent experiments [46,47] we remark that often the experimental situation is such, the incident light is only partially polarised. For this case a recipe has been suggested in Ref. [87] which express the measured cross-section $W(\Omega_a, \Omega_b, E_b)$ in terms of the linear (Eq. (3.37)) and the circular dichroism (Eq. (3.33)) LD_n and CD_n, respectively as

$$W(\Omega_a, \Omega_b, E_b) = \frac{\Sigma_c}{2}(1 + S_1 \text{LD}_n - S_3 \text{CD}_n)\,, \tag{3.52}$$

where the unpolarised cross-section Σ_c is given by $\Sigma_c = C\Sigma$ (cf. Eqs. (3.36) and (3.1)) and S_1 and S_3 are the Stokes parameters describing the degree of linear and circular polarisation, respectively. From Eq. (3.52) it is clear that for equal energy sharing of the two continuum electrons, the CD_n vanishes and the LD_n is directly accessible. This situation is illustrated in Fig. 7. In contrast, for the

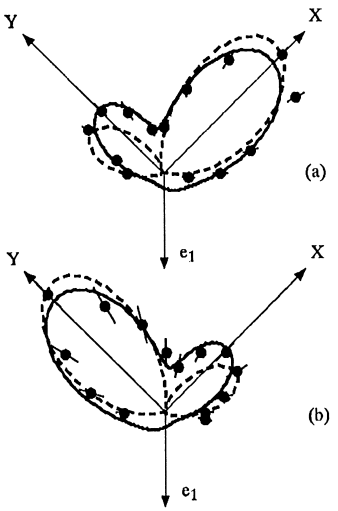

Fig. 9. The same experimental arrangement as in Fig. 8 with the same labelling of the curves and symbols. In (a) [(b)] is depicted the PDI cross-section following the absorption of right (left)-hand circularly polarised photon. The experimental data have been obtained from Fig. 8 by subtracting the S_1 part from the cross-sections. Thus the Stokes parameters in (a) are $S_1 = 0$, $S_3 = 0.95$ whereas in (b) they are $S_1 = 0$, $S_3 = -0.95$. Results are courtesy of Ref. [50].

case of unequal energy sharing both LD_n and CD_n are finite with a relative strength depending on the dynamics and, of course, on S_1 and S_2, as shown in Fig. 8. As demonstrated in Refs. [50,88], for a suitable choice of the Stokes parameters S_1 and S_3 one can subtract the part of the coincidence signal that is depending on S_1 and extract thus cross-sections solely due to the circular polarised photon and measure thus the circular dichroism, as illustrated in Fig. 9.

3.11. Circular dichroism in the Auger-electron photoelectron spectroscopy

Soon after the prediction of the circular dichroism in one-step double photoionisation it was pointed out that the same effect should be observable in photon-induced Auger processes [38,51,52]. In this part of the paper we give a brief account of the theory of circular dichroism in photon-induced Auger processes.

The exposure of an atom to circularly polarised light may result in an inner shell ionisation. The inner shell hole state may decay via emission of an Auger electron into a final stable ion. The two escaping electrons, the photoelectron and the Auger electron can then be detected in coincidence.

The emission intensity I of the Auger electrons escaping with a momentum $\boldsymbol{p}_a$ is [17,19,89]

$$I(\boldsymbol{p}_a) \propto \sum_{M_\mathrm{f} M M'} \langle J_\mathrm{f} M_\mathrm{f} \boldsymbol{p}_a | V | J M \rangle \rho(M, M') \langle J M' | V | J_\mathrm{f} M_\mathrm{f} \boldsymbol{p}_a \rangle \,, \tag{3.53}$$

where J and M are angular momentum and the magnetic quantum number of the innershell hole state whereas $J_\mathrm{f}, M_\mathrm{f}$ are the corresponding quantum numbers for the final ion state. Here we assume that the spin states of the Auger electron are not resolved. In addition, we sum over

M_f since the magnetic sublevels of the final ion are normally not detected. In Eq. (3.53) $\rho(M, M')$ is the density matrix of the inner shell hole state. The structure of $\rho(M, M')$ depends sensitively on the creation process of the hole state. In the present case this mechanism is the photoionisation. Therefore, the density matrix is basically given by the photoionisation probability,

$$\rho(M, M') = \frac{1}{2J_0 + 1} \sum M_0 \langle JM\boldsymbol{p}_p|\hat{\varepsilon}\cdot\boldsymbol{r}|J_0 M_0\rangle\langle J_0 M_0|\hat{\varepsilon}^*\cdot\boldsymbol{r}|JM\boldsymbol{p}_p\rangle \,, \tag{3.54}$$

where $J_0 M_0$ are the angular momentum quantum numbers of the initial state, $\hat{\varepsilon}$ is the light polarisation unit vector, $\boldsymbol{r}$ is the dipole operator in length form, and $\boldsymbol{p}_p$ is the momentum of the emitted photoelectron. A statistical average over the initial M_0-distributions has been performed as the target is not oriented. Using the re-coupling formula given by Eq. (3.6) we deduce for the difference Δ_a of cross-sections between right- and left-hand circular polarisation of the incident photon the expression

$$\Delta_a = \sum_{M_f M M'} \langle J_f M_f \boldsymbol{p}_a|V|JM\rangle\langle JM\boldsymbol{p}_p|\boldsymbol{r}\times\boldsymbol{r}'|JM'\boldsymbol{p}_p\rangle\langle JM'|V|J_f M_f \boldsymbol{p}_a\rangle \,. \tag{3.55}$$

Here we defined $\boldsymbol{r}' = P\boldsymbol{r}$ with $P = (1/(2J_0 + 1))\sum_{M_0}|J_0 M_0\rangle\langle J_0 M_0|$. It is essential that the vector product of the photoionisation amplitudes is not equal to zero. More detailed analysis of the features of the dichroism are given in Ref. [38].

At the end of this section we remark that there is a number of further promising theoretical and experimental techniques currently under development for the investigation of dichroic effects in double ionisation with polarised photons. Here we gave a compact account of the ideas, mostly concerned with two-electron atoms. However, the phenomenon of dichroism is far more reaching and should show up in a general electronic system. The behaviour of the dichroism in a correlated many-electron compounds is the subject of a future research.

4. Chiral electron pair emission from laser-pumped atoms

In Section 3, we investigated the chirality transfer from the radiation field to a correlated electron pair. The two-electron initial state prior to the photon absorption was randomly oriented. In this section we consider a situation in which the electron pair in the initial state possesses already an internal orientation. We study then the role of this orientation when the electron pair is excited into a continuum state. Experimentally, this reaction is realised by pumping a one-active electron atom, say an alkali atom, with circular polarised light to achieve a certain population of the magnetic sublevels M of the total angular momentum J. This population can be generally described by a density matrix ρ^J_{MM}. The prepared atomic target with well-defined sense of rotation of the excited electron is then ionised by a low-energy electron beam (the incident energy is typically a few times the ionisation potential of the target). The remaining residual ion is isotropic. Therefore, the sense of rotation that is present in the system before the ionisation event, is transferred to the two correlated continuum electrons.

In this section we shed light on the questions: (1) In which way the sense of orientation of the electronic motion modifies the ionisation dynamics, if at all. (2) What are the common features and

the differences between this case and the situation of chiral electron pairs from PDI. To this end we start by analysing the process using a formal tensorial analysis and exploring the symmetry properties that has to be imposed on the electron-impact ionisation process due to initial orbital orientation of the atomic electrons. Subsequently, we present a simple dynamical model within which closed analytic formula can be obtained. Finally, we discuss more elaborate scattering dynamic approaches and compare with experimental findings.

4.1. Formal development

The incoming electron beam with well-defined momentum $\boldsymbol{k}_0$ intersects the oriented and/or aligned atomic beam in the interaction region. Thereafter, two interacting continuum electrons leave simultaneously the interaction region. For the analysis of such an experiment we employ the density-matrix methodology that has been developed for the description of state-selective elastic and inelastic scattering experiments [60,91–93]. The atomic and electron beams are characterised by density operators whose matrix representations reflect the statistical mixture of pure states of the respective beam. The initial state of the system, consisting of the atom and the incoming electron beam, is described by a density operator ρ^{in} which is a direct product of the electron-beam density operators ρ^{e} and the density operator ρ of the laser-pumped atom. This is because the electron and atomic beams are initially prepared far from the interaction region, and as such are not correlated (long before the collision) [91] so that

$$\rho^{\mathrm{in}} = \rho^{\mathrm{e}} \times \rho \ . \tag{4.1}$$

For the sake of clarity we study a situation in which the initial electron beam is unpolarised. In this case, the reduced density matrix of the electron beam is simply the unit matrix [60] with the normalisation coefficient reflecting the dimension of the electron spin-space

$$\rho^{\mathrm{in}} = \frac{1}{2} \sum_{\substack{M,M' \\ v_0}} |v_0, J, M\rangle \rho^J_{M,M'} \langle v_0, J, M'| \ . \tag{4.2}$$

Usually, the atoms are laser-pumped into a specific hyperfine state $|F, M_F\rangle$ rather then into a total angular momentum state $|J, M\rangle$. However, as proposed by Percival and Seaton [94], the non-zero nuclear spin has no dynamical effect. It enters only through re-coupling coefficients that are dropped from relation (4.2). Thus, it suffices to consider the atomic beam prepared in the quantum states $|J, M\rangle$. The quantum number v_0 in Eq. (4.2) labels the electron spin projections.

The atomic beam is conveniently described in the photon frame where the quantisation axis $\hat{\boldsymbol{e}}_z$ is parallel to the beam's propagation direction in the case of a circularly polarised light and to the direction of the electric field in the case of a linearly polarised light [95]. In the photon frame the density matrix of the excited atomic state and of the ground state becomes diagonal.

In general, the angle- and energy-resolved cross-section $\bar{W}(\Omega_a, \Omega_b, E_b)$ for the simultaneous ejection of two electrons from an atomic target by an unpolarised electron beam is calculated as [90,97]

$$\bar{W}(\Omega_a, \Omega_b, E_b) = \kappa \sum_{\substack{v_0, M \\ M_{\mathrm{f}} v_a v_b}} \mathscr{M}(\boldsymbol{k}_a, v_a, \boldsymbol{k}_b, v_b, M_{\mathrm{f}}; JLM, \boldsymbol{k}_0) \rho^J_{MM} \mathscr{M}^{\dagger}(\boldsymbol{k}_a, v_a, \boldsymbol{k}_b, v_b, M_{\mathrm{f}}; JLM, \boldsymbol{k}_0) \ . \tag{4.3}$$

Here $\mathscr{M}$ is the matrix element of the transition operator T and is given by

$$\mathscr{M} = \langle \boldsymbol{k}_a v_a \boldsymbol{k}_b v_b \Phi^{\text{ion}}_{J_f L_f M_f} | T | \Phi^{\text{atom}}_{JLM} \boldsymbol{k}_0 v_0 \rangle ,$$

where $|\Phi^{\text{atom}}_{JLM}\rangle$ is the initial bound state of the atom and $|\Phi^{\text{ion}}_{J_f L_f M_f}\rangle$ is the state of the residual ion formed upon the ionisation event. Eq. (4.3) assumes no resolution of the spin projections v_a and v_b of the two outgoing electrons. The kinematical factor κ in Eq. (4.3) is given by

$$\kappa = (2\pi)^4 \frac{k_f k_s}{k_0} . \tag{4.4}$$

For a systematic analysis of the process it is useful to separate properties that are related to the initial state preparation from those concerning the collision dynamics. This can be conveniently achieved when the density matrix ρ^J_{MM} is expressed in terms of its state multipoles ρ_{KQ}, i.e. in terms of statistical tensor components [60]

$$\rho^J_{MM} = \sum_K (-1)^{K-J-M} \langle J - MJM | K0 \rangle \rho_{KQ=0} , \tag{4.5}$$

where K and Q in relation (4.5) stand for, respectively, the rank of the statistical tensor and its projection along the quantisation axis. As seen from relation (4.5) only the $Q = 0$ components of the state multipoles contributes to expansion (4.5). This is a result of the density matrix being diagonal in the photon frame (in which we are operating). Using relations (4.3) and (4.5) the cross-sections can be expressed in terms of irreducible tensor components as [99]

$$\bar{W}(\Omega_a, \Omega_b, E_b) = \sum_{K=0}^{2J} \rho_{K0} \Lambda^{(K)}_0 . \tag{4.6}$$

This expression has the desirable feature that the geometry of the experiment, as described by the state multipoles, is completely disentangled from the reaction dynamics (contained in the tensorial parameters $\Lambda^{(K)}_0$). The components $\Lambda^{(K)}_0$ read

$$\Lambda^{(K)}_0 = C \sum_{\substack{v_0, M \\ M_f v_a v_b}} (-)^{J+M+K} \langle J - MJM | K0 \rangle \mathscr{M} \mathscr{M}^\dagger . \tag{4.7}$$

That the parameters $\Lambda^{(K)}_0$ can in fact be regarded as the components of a tensor of rank K can be seen as follows: The M dependence of the matrix element $\mathscr{M}(M)$ is solely due to the dependence on the magnetic sublevels of the initial state which is an eigenstate of an angular momentum. Therefore, $\mathscr{M}(M)$ may be considered as the Mth component of a spherical tensor. Further, we can write the complex conjugate in the form $(\mathscr{M}(M))^* = (-)^{p-M} \mathscr{W}(-M)$. This relation is a definition for the tensor $\mathscr{W}$, and resembles formally the definition of the adjoint of a tensor operator where the phase p is arbitrary [69] except that $p - M$ must be an integer.

The association of the parameters $\Lambda^{(K)}_0$ with spherical tensors has important consequences for the symmetry properties with respect to rotations: The quantity $\Lambda^{(K)}_0$ is scalar under overall rotations whereas $\Lambda^{(K=\text{odd})}_0$ is an orientation and hence changes sign upon reflection of the quantisation axis. The parameters $\Lambda^{(K=\text{even})}_0$ are alignment parameters. A further important property of the classification (4.6) is the finite number of contributing $\Lambda^{(K)}$'s. This number is given by $2J + 1$ where J is the total angular momentum of the target atom, e.g. for $J = 0$ we get neither an orientation nor an

alignment, $J = 1/2$ allows for an orientation but not for an alignment, and for $J \geq 1$ we expect in general both an orientation and an alignment. The scalar, for instance, corresponding to $K = 0$ is nothing else but the cross-section averaged over the statistical M-population

$$\Lambda_0^{(0)} = (2J+1)^{-1/2} C \sum_{\substack{\nu_0, M \\ M_f \nu_a \nu_b}} \mathscr{M}\mathscr{M}^\dagger \tag{4.8}$$

and

$$\rho_{00} = (2J+1)^{-1/2} . \tag{4.9}$$

For $K = 1$ one obtains the vectorial orientation

$$\Lambda_0^{(1)} = \sqrt{\frac{3}{J(J+1)(2J+1)}} C \sum_{\substack{\nu_0, M \\ M_f \nu_a \nu_b}} M \mathscr{M}\mathscr{M}^\dagger$$

and the state multipole

$$\rho_{10} = \sqrt{\frac{3}{J(J+1)(2J+1)}} \sum_M M \rho_{MM}^{(J)} .$$

The simplest application of the above formalism is the low-energy electron-pair ejection from a light target atom with one active electron, such as sodium. Relativistic interactions that may alter the spin projections of the continuum electrons without conservation of the total spin of the system are then neglected. The spatial and the spin part of the T-matrix elements can be decoupled. In the case of a sodium target Eq. (4.6) can be expanded as [58,99]

$$\bar{W}(\Omega_a, \Omega_b, E_b) = \tfrac{1}{3}\Lambda_0^{(0)} + \tfrac{1}{\sqrt{2}}(\rho_{11}^{(1)} - \rho_{-1-1}^{(1)})\Lambda_0^{(1)} + \tfrac{1}{\sqrt{6}}(1 - 3\rho_{00}^{(1)})\Lambda_0^{(2)} . \tag{4.10}$$

As mentioned above, the tensorial components along the quantisation axis of the target are functions of the state-resolved cross-sections, σ_{L,m_L}, e.g.

$$\Lambda_0^{(0)} = \frac{\kappa}{\sqrt{3}}(\sigma_{1,1} + \sigma_{1,0} + \sigma_{1,-1}) , \tag{4.11}$$

$$\Lambda_0^{(1)} = \frac{\kappa}{\sqrt{2}}(\sigma_{1,1} - \sigma_{1,-1}) , \tag{4.12}$$

$$\Lambda_0^{(2)} = \frac{\kappa}{\sqrt{6}}(\sigma_{1,1} - 2\sigma_{1,0} + \sigma_{1,-1}) . \tag{4.13}$$

The cross-sections, σ_{L,m_L}, are deduced from the matrix element of the singlet $T(S=0)$ and the triplet $T(S=1)$ transition operator where S is the total spin of the electron pair:

$$\sigma_{L,m_i} = \kappa \sum_S \frac{1}{2S+1} |\langle \boldsymbol{k}_a \nu_a \boldsymbol{k}_b \nu_b \Phi_{L_i M_i}^{\text{ion}} | T^S | \Phi_{LM}^{\text{atom}} \boldsymbol{k}_0 \nu_0 \rangle|^2 . \tag{4.14}$$

These relations render possible the calculations of the state-selective cross-sections for arbitrary orientation of the momentum transfer vector, $\boldsymbol{q} = \boldsymbol{k}_0 - \boldsymbol{k}_a$ with respect to the quantisation axis, $\hat{\boldsymbol{e}}_z$ [102].

4.2. Symmetry relations of the orientational dichroism

As we discussed above the parameter $A_0^{(1)}$ quantifies the sensitivity of the cross-section to the inversion of the helicity of the exciting laser. Therefore, we term it *orientational dichroism*. Here we consider some exact symmetry properties that can be used as a benchmark for experimental and theoretical studies. To do this we omit from the discussion the internal structure of the residual ion.

The initial ($\Phi_{k_0,nLM}(\boldsymbol{r}_a,\boldsymbol{r}_b)$) and the final states ($\Psi^-_{\boldsymbol{k}_a,\boldsymbol{k}_b}(\boldsymbol{r}_a,\boldsymbol{r}_b)$) are solutions of the same six-dimensional Schrödinger equation, however with different boundary conditions (an incoming free electron and an oriented electron bound to an ion in case of $|\Phi_i\rangle$ and two interacting electrons in the field of a positive ion in case of $|\Psi^-_{\boldsymbol{k}_a,\boldsymbol{k}_b}\rangle$). The Schrödinger equation is a second-order differential equation in the coordinate space that treats the two electrons symmetrically. Besides, the (Coulomb) potentials of concern here are exclusively scalar. Therefore, we deduce

$$\Psi^-_{\boldsymbol{k}_a,\boldsymbol{k}_b}(\boldsymbol{r}_a,\boldsymbol{r}_b) = \Psi^-_{\boldsymbol{k}_b,\boldsymbol{k}_a}(\boldsymbol{r}_b,\boldsymbol{r}_a)\,,$$

$$\Psi^-_{-\boldsymbol{k}_a,-\boldsymbol{k}_b}(-\boldsymbol{r}_a,-\boldsymbol{r}_b) = \Psi^-_{\boldsymbol{k}_a,\boldsymbol{k}_b}(\boldsymbol{r}_a,\boldsymbol{r}_b)\,. \tag{4.15}$$

Same relations as (4.15) applies to $\Phi_{k_0,nLM}(\boldsymbol{r}_a,\boldsymbol{r}_b)$. Therefore, we conclude for the transition matrix elements (the perturbation operators are scalar operators)

$$\mathcal{M}(M,\boldsymbol{k}_a,\boldsymbol{k}_b,\boldsymbol{k}_0) = \mathcal{M}(M,\boldsymbol{k}_b,\boldsymbol{k}_a,\boldsymbol{k}_0)\,, \tag{4.16}$$

$$\mathcal{M}(-M,-\boldsymbol{k}_a,-\boldsymbol{k}_b,-\boldsymbol{k}_0) = \mathcal{M}(M,\boldsymbol{k}_b,\boldsymbol{k}_a,\boldsymbol{k}_0)\,. \tag{4.17}$$

Furthermore, the laser-pumped initial state possesses a cylindrical symmetry around the quantisation axis. A reflection at the (z–x)-plane should not modify the initial state. Hence, the relation applies

$$\mathcal{M}(-M,\boldsymbol{k}_a,\boldsymbol{k}_b,\boldsymbol{k}_0) = \mathcal{M}(M,\boldsymbol{k}'_b,\boldsymbol{k}'_a,\boldsymbol{k}'_0)\,, \tag{4.18}$$

where $\boldsymbol{k}'_0,\boldsymbol{k}'_b$ and $\boldsymbol{k}'_a$ are the momenta of the incoming and two outgoing electrons being reflected at the $(z-x)$-plane. The relation Eq. (4.18) is of course only valid if the prepared electronic state of the atom is a pure state with a cylindrical symmetry around the quantisation axis.

Eq. (4.18) requires a vanishing $A_0^{(1)}$ when $\boldsymbol{k}'_0,\boldsymbol{k}'_b,\boldsymbol{k}'_a$ and $\hat{\boldsymbol{e}}_z$ are in the same plane, for we can always choose the x-axis to lay in this same plane and therefore we obtain $\boldsymbol{k}'_0=\boldsymbol{k}_0$, $\boldsymbol{k}'_b=\boldsymbol{k}_b$, $\boldsymbol{k}'_a=\boldsymbol{k}_a$. Moreover, in certain circumstances symmetry properties of the tensorial parameters could be inferred from relation (4.18). For example, we choose $\boldsymbol{k}_0,\boldsymbol{k}_a$ to lie in the (z–x)-plane and consider the $A_0^{(K)}$ as function of the azimuthal angle φ_b associated with $\boldsymbol{k}_b$ (the polar angle and the energy of electron "b" θ_b and E_b are fixed). Obviously, Eq. (4.18) requires $\mathcal{M}(-M,\varphi_b)=\mathcal{M}(M,2\pi-\varphi_b)$, i.e. $A_0^{(1)}(\varphi_b) = -A_0^{(1)}(2\pi-\varphi_b)$ which means that $A_0^{(1)}(\varphi_b)$ is an odd function with respect to φ_b. In addition, the following relations for $A_0^{(0)}(\varphi_b)$ are easily inferred

$$\begin{aligned} A_0^{(0)}(\varphi_b) &= \frac{C}{\sqrt{3}}\sum_{m=-1}^{1}|\mathcal{M}^{(m)}(\varphi_b)|^2 \\ &= \frac{C}{\sqrt{3}}\sum_{m=-1}^{1}|\mathcal{M}^{(-m)}(2\pi-\varphi_b)|^2 = A_0^{(0)}(2\pi-\varphi_b)\,. \end{aligned} \tag{4.19}$$

A similar relation holds for $\Lambda_0^{(2)}(\varphi_b)$ as well. These transformational symmetry properties of $\Lambda_0^{(K)}(\varphi_b)$, $K = 0, 1, 2$ are independent of the employed approximations for the scattering dynamics. However, the magnitude and shape of $\Lambda_0^{(K)}$, $K = 1, 2, 3$ is largely affected by the description of the collision dynamics [99,102].

4.3. Analytical results

To get some insight into the general properties of the orientational dichroism it is instructive to consider dynamical models for which the dichroism can be evaluated analytically. The simplest theoretic approach for which $\Lambda_0^{(1)}$ is finite and can be deduced analytically is the first Born approximation (FBA) for the ionisation of an alkali atom. The FBA performs reasonably well for fast collisions accompanied by small values of momentum transfer $\boldsymbol{q} = \boldsymbol{k}_0 - \boldsymbol{k}_a$ [96]. Within the FBA one of the escaping electrons (electron "a" in our notation) propagates freely whereas the slow electron is assumed to be subject to the field of the residual ion. The final state wave function is obtained from Eq. (3.40) upon the replacement $\beta_a \equiv 0$. Within the FBA the transition matrix elements are evaluated as

$$\mathscr{M}_{\mathrm{FBA}}^{(m)} = \frac{1}{2\pi^2 q^2}\langle \psi_{\boldsymbol{k}_b}(\boldsymbol{r})|\exp(\mathrm{i}\boldsymbol{q}\cdot\boldsymbol{r})|\phi_{nlm}(\boldsymbol{r})\rangle \,, \tag{4.20}$$

where $\psi_{\boldsymbol{k}_b}(\boldsymbol{r})$ is a one-electron continuum wave function of the alkali atom which is orthogonal to the bound state $\phi_{nlm}(\boldsymbol{r})$ of the valence electron. Here $\boldsymbol{r}$ is the position of the bound electron with respect to the nucleus. To keep the number of the tensorial parameters small we consider a p state for which $K = 0, 1, 2$. The bound p-state wave function can be written in the form $\varphi_{n1m}(\boldsymbol{r}) = R_{np}(r)\mathscr{Y}_{1m}(\boldsymbol{r})$ with $\mathscr{Y}_{lm}(\boldsymbol{r}) = \sqrt{4\pi/(2l+1)}r^l Y_{lm}(\hat{\boldsymbol{r}})$. Here Y_{lm} is being a standard spherical harmonic. Expressing the scalar product $\boldsymbol{q}\cdot\boldsymbol{r}$ in terms of spherical vector components

$$\boldsymbol{q}\cdot\boldsymbol{r} = \sum_m (-)^m q_m r_{-m}$$

we rewrite the FBA-transition matrix elements as

$$\mathscr{M}_{\mathrm{FBA}}^{(m)} = -\mathrm{i}(-)^m \frac{1}{2\pi^2 q^2}\frac{\partial}{\partial q_{-m}}\langle \psi_{\boldsymbol{k}_b}(\boldsymbol{r})|\mathrm{e}^{\mathrm{i}\boldsymbol{q}\cdot\boldsymbol{r}}|R_{np}(r)\rangle \,. \tag{4.21}$$

Because the matrix element in Eq. (4.21) depends only on q^2 and $\boldsymbol{k}_b\cdot\boldsymbol{q}$ the Born transition matrix element has the structure

$$\mathscr{M}_{\mathrm{FBA}}^{(m)} = (\alpha\boldsymbol{q} + \beta\boldsymbol{k}_b)_m \,, \tag{4.22}$$

where the index m refers to a spherical vector component, and the dynamical parameters α and β are independent of m. Thus, within the FBA the quantities $\Lambda_0^{(K)}$ evaluate to

$$\Lambda_0^{(0)} = \frac{C}{\sqrt{3}}[|\alpha|^2 q^2 + |\beta|^2 k_b^2 + 2\mathrm{Re}(\alpha\beta^*)\boldsymbol{q}\cdot\boldsymbol{k}_b] \,, \tag{4.23}$$

$$\Lambda_0^{(1)} = \frac{C}{\sqrt{2}}\mathrm{Im}(\alpha\beta^*)(\boldsymbol{q}\times\boldsymbol{k}_b)\cdot\hat{\boldsymbol{e}}_z \ , \tag{4.24}$$

$$\Lambda_0^{(2)} = \frac{C}{\sqrt{6}}[|\alpha|^2(q^2-3q_0^2)+|\beta|^2(k_b^2-3k_{b0}^2)+2\mathrm{Re}(\alpha\beta^*)(\boldsymbol{q}\cdot\boldsymbol{k}_b-3q_0k_{b0})] \ , \tag{4.25}$$

where $k_{b0}=\boldsymbol{k}_b\cdot\hat{\boldsymbol{e}}_z$. The tensor components (4.23)–(4.25) have the following geometrical symmetry properties. Because α and β depend on the scalars q, k_b and $\boldsymbol{q}\cdot\boldsymbol{k}_b$ we recover the well-known fact that $\Lambda_0^{(0)}$ is cylindrically symmetric around the direction of $\boldsymbol{q}$. Further, recalling that $\hat{\boldsymbol{e}}_z$ is a unit vector along the angular momentum quantisation axis we deduce that one of the necessary conditions for a finite value of $\Lambda_0^{(1)}\propto\hat{\boldsymbol{e}}_z\cdot(\boldsymbol{q}\times\boldsymbol{k}_b)$ is the linear independence of the three vectors $\hat{\boldsymbol{e}}_z$, the momentum transfer $\boldsymbol{q}$ and the momentum of the secondary electron $\boldsymbol{k}_b$. The orientation $\Lambda_0^{(1)}$ vanishes if these three vectors are coplanar. It changes sign if the orientation of the frame formed by $\hat{\boldsymbol{e}}_z,\boldsymbol{q},\boldsymbol{k}_b$ is inverted. In particular, we find a reflection-anti-symmetry of $\Lambda_0^{(1)}$ with respect to $\theta_q=\cos^{-1}\hat{\boldsymbol{q}}\cdot\hat{\boldsymbol{k}}_b$. Sufficient conditions for $\Lambda_0^{(2)}=0$ are summarised by $(\hat{\boldsymbol{q}}\cdot\hat{\boldsymbol{e}}_z)^2=1/3$, $(\hat{\boldsymbol{k}}_b\cdot\hat{\boldsymbol{e}}_z)^2=1/3$ and $\hat{\boldsymbol{q}}\cdot\hat{\boldsymbol{k}}_b=3(\hat{\boldsymbol{q}}\cdot\hat{\boldsymbol{e}}_z)(\hat{\boldsymbol{k}}_z\cdot\hat{\boldsymbol{e}}_z)$. This means, $\Lambda_0^{(2)}=0$ if $\boldsymbol{q}\|\boldsymbol{k}_b$ and both ($\boldsymbol{q}$ and $\boldsymbol{k}_b$) of them form a magic angle of $\theta_{\mathrm{mag}}=\cos^{-1}1/\sqrt{3}$ or $\pi-\theta_{\mathrm{mag}}$ with the angular momentum quantisation axis, $\hat{\boldsymbol{e}}_z$. The portion $\Lambda_0^{(2)}$ vanishes also if $\boldsymbol{q}\|-\boldsymbol{p}_b$ and one of these vectors forms a magic angle θ_{mag} with $\hat{\boldsymbol{e}}_z$ while the other one has a magic angle of $\pi-\theta_{\mathrm{mag}}$ with $\hat{\boldsymbol{e}}_z$. If $\boldsymbol{q}$ and $\boldsymbol{k}_b$ are perpendicular to $\hat{\boldsymbol{e}}_z$, Eqs. (4.23) and (4.25) yield

$$\Lambda_0^{(2)} = \frac{1}{\sqrt{2}}\Lambda_0^{(0)} \tag{4.26}$$

and hence $\mathcal{M}_{\mathrm{FBA}}^{(m=0)}=0$.

As clear from Eq. (4.24) the orientational dichroism is absent when the dynamical factor $\mathrm{Im}(\alpha\beta^*)$ vanishes. This fact has been investigated in Ref. [103]. In that work it has been possible to deduce analytically the condition under which the term $(\alpha\beta^*)$ is zero and therefore $\Lambda_0^{(1)}=0$, more details can be found in Ref. [103].

The FBA simplifies to the plane-wave impulse approximation (PWIA) when both final-state electrons are considered as moving free in the field of the residual ion. Within the PWIA the transition matrix elements reduce to

$$M_{\mathrm{PWIA}}^{(m)} = \mathrm{i}(\gamma\boldsymbol{k}_b+\eta(\boldsymbol{q}-\boldsymbol{k}_b))_m = \mathrm{i}(\gamma'\boldsymbol{k}_b+\eta\boldsymbol{q})_m \tag{4.27}$$

with γ' and η being real. This has the important consequence that the orientation $\Lambda_0^{(1)}$ is equal to zero. Thus, the orientation of two continuum electrons is expected to decline for fast escaping electrons because the PWIA would then be a satisfactory approximation. The two other quantities $\Lambda_0^{(0)}$ and $\Lambda_0^{(2)}$, however, are in general finite.

4.4. Calculational schemes and experimental findings

As in the case of double ionisation by a circular photon, the tensorial analysis can provide information as to the transformation properties of the cross sections and can help express the measurable quantities in terms of independent mathematical objects that characterise certain aspects of the chiral multi-electron emission. To evaluate these objects one encounters the problem of dealing

with the correlated few-body scattering states. In Section 3.9 we presented a method for the calculations of cross-sections. Basically, these methods can be applied here as well. However, only the 3C method has been used in addition to two other theories that are discussed in this section. Since the experiment is focused on atomic sodium as a target we discuss the theories and their results in light of the reaction $\gamma_{\sigma^\pm} + \mathrm{Na} \to \mathrm{Na}(3^2P_{3/2}, F = 3, m_F = \pm 3) + e^- \to \mathrm{Na}^+ + e^- + e^-$. All theories on the market describes the sodium atom as an effective one-electron atom.

One standard method in atomic scattering theory that has been applied to the present problem is the distorted wave Born approximation (DWBA) [97,98]. This method accounts for the short- and long-range interactions in both the initial and the final channels but treats the two outgoing electrons as being independent. Within the DWBA the total Hamiltonian H of the projectile-electron and the target is written as

$$H = h_1 + h_2 + v_{12} \,, \tag{4.28}$$

where h_1 and h_2 are the Hamiltonians of the two electrons participating in the scattering process. The operators h_1 and h_2 consist of the individual kinetic energy operators K_i and the one-particle potentials V_i. The electron–electron interaction potential missing in V_i is referred to as v_{12}.

Within the framework of the DWBA, the collision Hamiltonian is split as [97,98]

$$H = (K_1 + U_1 + K_2 + V_2) + (V_1 + v_{12} - U_1) \,, \tag{4.29}$$

$$= K + V \,, \tag{4.30}$$

where U_1 is the distorting potential which has still to be defined [104]. The (unsymmetrised) transition matrix elements are approximately given by

$$\langle \boldsymbol{k}_a \boldsymbol{k}_b \Phi^{\mathrm{ion}}_{J_\mathrm{f} L_\mathrm{f} M_\mathrm{f}} | T | \Phi^{\mathrm{atom}}_{JLM} \boldsymbol{k}_0 \rangle \equiv \langle \chi^{(-)}(\boldsymbol{k}_a) \chi^{(-)}(\boldsymbol{k}_b) | V | \phi_{LM} \chi^{(+)}(\boldsymbol{k}_0) \rangle \,. \tag{4.31}$$

The one-electron orbital of the active target electron is labelled by ϕ_{LM}. The distorted waves, $\chi^{(\pm)}(\boldsymbol{k})$, are one-electron states and are derived as scattering solutions of the one-particle channel Hamiltonian K. The radial part of the distorted waves is derived as a solution of a radial second-order differential equation of the type

$$\left[\frac{\mathrm{d}^2}{\mathrm{d}r^2} - \frac{l(l+1)}{r^2} - 2v(r) + k^2 \right] u_l(r) = 0 \,. \tag{4.32}$$

In relation (4.32), the potential $v(r)$ corresponds to the distorting potential. In the example shown below this potential is chosen as the equivalent-local static-exchange potential of Furness and McCarthy [105] to describe the scattering in the field of the atom. The corresponding local static-exchange potential for the ion is chosen, in addition to the Coulomb potential, when the distorted waves are considered as electron–ion states.

We remark that in both alternatives of the DWBA the electron–electron interaction is not included in the calculation of the outgoing distorted waves. Thus, the bound-electron orbital and the distorted waves representing the slow escaping electron are orthogonal. Therefore, only the electron–electron interaction potential v_{12} contributes to Eq. (4.32).

A further scattering approach that has been applied to this problem is the dynamically screened three coulomb waves method (DS3C) [76]. Within this method, the transition matrix elements are

approximated as

$$\langle \boldsymbol{k}_a \boldsymbol{k}_b \Phi^{\text{ion}}_{J_f L_f M_f} | T | \Phi^{\text{atom}}_{JLM} \boldsymbol{k}_0 \rangle \equiv \langle \Psi^{(-)}_{(\boldsymbol{k}_a,\boldsymbol{k}_b)} | V | \phi_{L,M_L} \boldsymbol{k}_0 \rangle \ . \tag{4.33}$$

In relation (4.33), the initial state of the electron–atom system is chosen as a product of a plane wave describing the incoming projectile and a bound state describing the laser-excited atom state. The perturbation V is that part of the total potential of the electron–atom system which is not diagonalised by the state vector $|\phi_{L,M_L} \boldsymbol{k}_0\rangle$ (strictly speaking, this is only valid when the state vector $\langle \Psi^{(-)}_{(\boldsymbol{k}_a,\boldsymbol{k}_b)}|$ is an exact solution of the many-body problem consisting of the interacting atom and the projectile electron at the time of the collision). To make the numerical calculations of the transition matrix element tractable one has to assume that the residual ion (Na^+) acts in the final state as a positive unit point charge ($Z_{Na^+} = 1$). For the case of Na this assumption seems plausible and ensures correct boundary conditions. We mention however, that when the final state electrons are scattered nearby the nucleus the assumption of a unit point charge of Na^+ becomes questionable.

In Section 3.9, we discussed the problems associated with the description of many-body scattering states and presented the 3C wave function (3.48) as one of the possible approximate solutions. However, as mentioned previously the 3C model lacks the coupling between the individual two-body subsystems. This coupling might be very strong, especially at lower energies, e.g., the 3C model yields a threshold law [106,107] at variance with the Wannier theory [71] prediction and the experimental data close to the ionisation threshold. To circumvent this problem one is obliged to account for the three-particle correlation [76], i.e. the coupling between a two-body system and a third particle. This has been achieved by introducing an interaction strength within the two-body subsystems that is dependent on the positions of all particles. As can be expected this brings about delicate numerical problems as far as the evaluation of scattering amplitudes is concerned. However, for the electron-impact ionisation case it turned out that the position dependence of the two-particle interactions can be approximately converted into a functional dependence on the momenta. The resulting wave function has exactly the same functional form as Eq. (3.48), however the Sommerfeld parameters have now the form $\beta_j := Z_j/k_j$, $j = a, b$, and $\beta_{ab} := Z_{ab}/2k_{ab}$, where the product charges have been derived to be (for more detail cf. Refs. [76,100,101])

$$Z_{ba}(\boldsymbol{k}_a, \boldsymbol{k}_b) = [1 - (f\,g)^2 a^{b_1}] a^{b_2} \ , \tag{4.34}$$

$$Z_a(\boldsymbol{k}_a, \boldsymbol{k}_b) = -1 + (1 - Z_{ba}) \frac{k_a^{1+a}}{(k_a^a + k_b^a)|\boldsymbol{k}_a - \boldsymbol{k}_b|} \ , \tag{4.35}$$

$$Z_b(\boldsymbol{k}_a, \boldsymbol{k}_b) = -1 + (1 - Z_{ba}) \frac{k_b^{1+a}}{(k_a^a + k_b^a)|\boldsymbol{k}_a - \boldsymbol{k}_b|} \ . \tag{4.36}$$

The functions occurring in Eqs. (4.34) and (4.35) are defined as

$$f := \frac{3 + \cos^2(4\alpha)}{4}, \qquad \tan\alpha = \frac{k_a}{k_b} \ , \tag{4.37}$$

$$g := \frac{|\boldsymbol{k}_a - \boldsymbol{k}_b|}{k_a + k_b} \ , \tag{4.38}$$

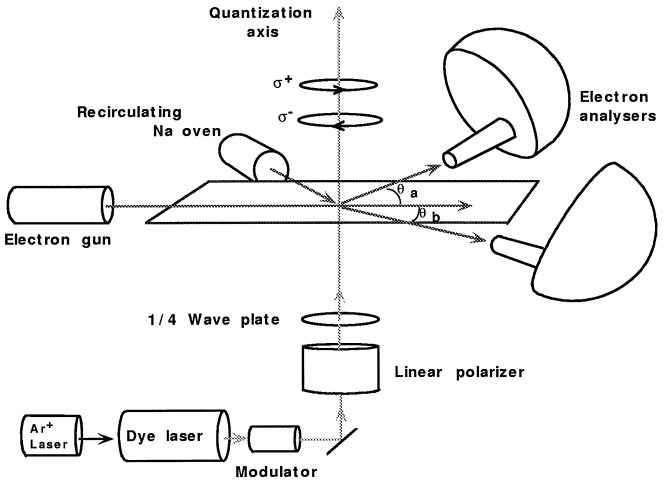

Fig. 10. A schematic representation of the experimental set-up for the measurement of the orientational dichroism in electron impact ionization of circular electronic state.

$$b_1 := \frac{2k_a k_b \cos(\theta_{ab}/2)}{k_a^2 + k_b^2} , \tag{4.39}$$

$$b_2 := g^2(-0.5 + \mu) , \tag{4.40}$$

$$a := \frac{E}{E + 0.5} . \tag{4.41}$$

Here E is being measured in atomic units and $\mu = 1.127$ is the Wannier index for $Z_{Na^+} = 1$. The interelectronic relative angle θ_{ab} is given by $\theta_{ab} := (\cos^{-1}\hat{\boldsymbol{k}}_a \cdot \hat{\boldsymbol{k}}_b)$.

From Eqs. (4.34)–(4.36) it is clear that when two particles approach each other (in momentum space) they experience their full two-body Coulomb interactions, whereas the third one 'sees' a net charge equal to the sum of the charges of the two close particles. When the two electrons recede from the residual ion (Na^+) in opposite directions and equal velocities (with respect to Na^+) the electron–electron interaction is subsumed completely in an effective electron–ion interaction. In addition, it can be shown that the behaviour of the total ionisation cross-sections evaluated using the final state function Eq. (3.48) with the product charges Eqs. (4.34)–(4.36) is compatible with the Wannier threshold law.

The experiments have been performed using the set-up shown schematically in Fig. 10. A coplanar asymmetric scattering geometry is chosen in which the momentum vectors $\boldsymbol{k}_0$, $\boldsymbol{k}_a$ and $\boldsymbol{k}_b$ of the incident and two final state continuum electrons of respective energies E_0, E_a and E_b are confined to a common plane. The angles θ_a and θ_b are measured with respect to the incident beam (cf. Fig. 10). In addition, a target beam of sodium atoms is produced by effusion of sodium gas through an aperture positioned at the output stage of a recirculating oven [102]. Intersecting at right angles the plane defined by the electron and sodium beams, and completely encompassing the region formed by their overlap, is a 589 nm laser beam used to excite the sodium atoms. The

initially linearly polarised laser light is converted to circularly polarised radiation by transmission through a quarter wave plate, the rotation of which by 90° reverses the helicity of the radiation field.

The coincidence rate is measured for two different helicities of the laser light and thus the orientational dichroism can be determined, as done in Fig. 11.

In Fig. 11 the DWBA results are shown along with the FBA ones. Since the scattering geometry is quite favourable for the application of the FBA (moderately high incident energy and small momentum transfer) the experimental data are reproduced satisfactorily well by the FBA, even though some details, such as the small shoulder in the angular distribution, is only reproduced by the DWBA calculations. As clear from the analytic results within the FBA, the orientational dichroism (the difference between the solid and the dotted curves) shows a reflection antisymmetry at the transfer momentum direction $\boldsymbol{q}$ and thus diminishes at the position of $\boldsymbol{q}$. This symmetry property is well confirmed by the experiment. The results for a hydrogenic target Fig. 11 differs only slightly from those for atomic sodium. This indicates that the picture of considering the sodium target as an effective one electron atom is adequate for present purposes. In Fig. 11 also shown are the calculations of the PWIA. Here the orientational dichroism vanishes identically, as discussed above. We note a double peak structure. The origin of this structure is the nodal structure of the initial bound state that leads to the minimum located at $\boldsymbol{q}$. This minimum in the angular distribution is basically the origin for the two peaks in the PWIA. Both the FBA and the PWIA (and in fact the DWBA) become less accurate when lowering the incident energy, as done in Fig. 12. Here we see a considerable break of the symmetry (around $\boldsymbol{q}$), as anticipated by the FBA for the orientational dichroism. Furthermore, it is clear from Fig. 12, that there is a subtle interplay between the final-state correlations (included in the final-state wave functions) and the sense of rotation of the initially bound electron. In fact, in this paricular case of Fig. 12, only the DS3C model reproduces the features of the orientational dichroism. This is consistent with the conclusions of previous studies on the ionisation of randomly oriented atoms [106,100,101] where the 3C model shows significant shortcomings at low energies (as compared to the experiments and the DS3C model).

The situation shown in Fig. 12 is in contrast to the one observed in the case of PDI where the propensity rules and the symmtery properties of the circular dichroism is valid irrespective of the modelling of the scattering dynamics.

It is the subject of current research to understand the physical mechanisms that underlies the strong effects of the orientation of the target on the electron pair emission at lower energies.

Further current and future research in this field are focused on the role of the spin in the emission process. First results can be found in Refs. [108,109].

5. Conclusions and outlook

In this work we discussed conceptual and numerical methods for the analysis and the treatment of chirality effects in multi-electron emission. A brief account of the chiral single-electron photoemission served as an introduction to the subject. In this case the chirality of the experimental set-up is caused by an initial orientation of the target or by specifying a certain projection of the photoelectron's spin. The chirality of the experiment is then changed by inverting the initial state

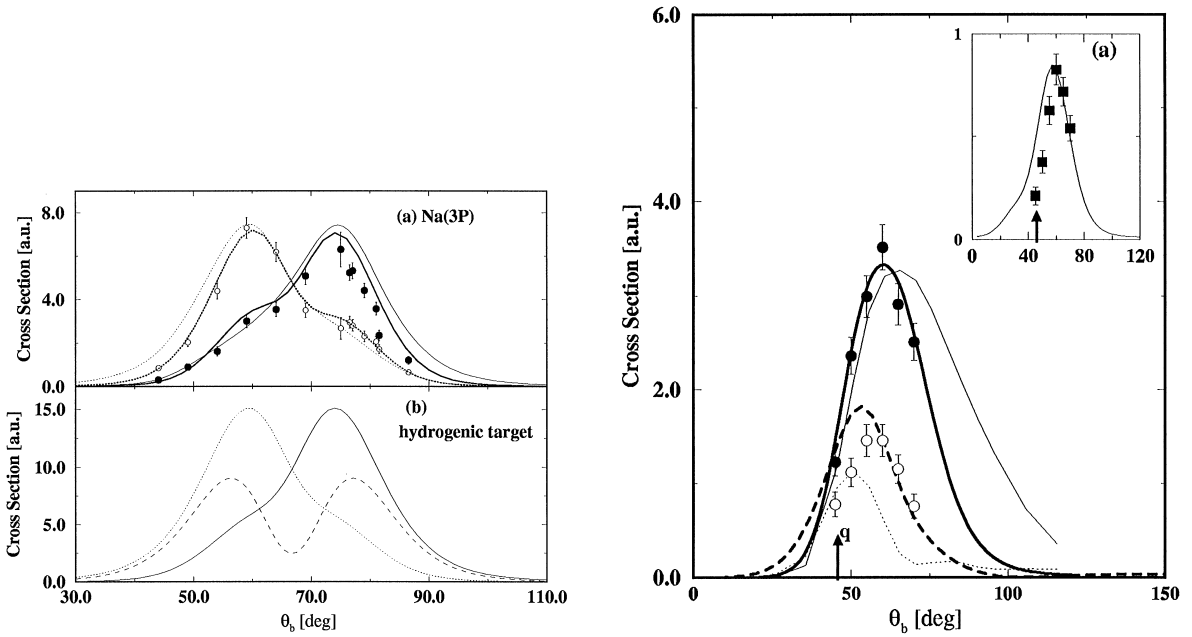

Fig. 11. The state-resolved cross-sections $\sigma_{L=1,m_L=\pm1}$ for the ionisation of atomic sodium (a) and atomic hydrogen (b). The experimental arrangement is depicted in Fig. 10. The x-axis is chosen as the wave vector of the pumping laser whereas the incoming beam defines the z direction. The polar angle of the scattered electron is fixed to $\theta_a = 20^\circ$ whereas the polar angle of the ejected electron θ_b is varied. The azimuthal angles are $\varphi_a = 180^\circ$ and $\varphi_b = 0^\circ$. The impact energy and the energy of the ejected electron are, respectively, $E_0 = 150\,\text{eV}$ and $E_b = 20\,\text{eV}$. In (a) the cross-sections $\sigma_{L=1,m_L=\pm1}$ for a Na(3P) target are calculated within the FBA ($\sigma_{L=1,m_L=-1}$ (thin solid line); $\sigma_{L=1,m_L=1}$ (thin dotted line)) and the DWBA theory [$\sigma_{L=1,m_L=-1}$ (solid line); $\sigma_{L=1,m_L=1}$ (dotted line)]. Experimental data are from Ref. [58]. In (b) the corresponding calculations are shown for a hydrogenic target: FBA($m_L = -1$) (solid line), FBA($m_L = 1$) (dotted line) and PWIA (dashed line).

Fig. 12. The electron impact ionisation cross-section for the scattering of 60 eV electrons from Na$3^2P_{3/2}$ $m_F = -3$ (filled circles) and $m_F = +3$ (open circles). The scattering geometry is shown in Fig. 11. The scattering angle is $\theta_a = 20^\circ$, $\phi_a - \phi_b = \pi$ and $E_b = 20\,\text{eV}$. The DS3C cross-sections are indicated by thick solid ($m_F = -3$) and thick dotted lines ($m_F = +3$) whereas the 3C results are shown as the thin solid ($m_F = -3$) and dotted lines ($m_F = +3$) (the 3C results are multiplied by a factor of 1.5). The measurements are normalised to the $m_F = -1$ DS3C cross-section peak. The momentum transfer direction is indicated by the arrow $\boldsymbol{q}$. The inset shows the ground state Na$3^2S_{1/2}$ transition normalised to the DS3C cross-section.

orientation or by flipping the photoelectron spin projection. The dependence of the photoelectron spectrum on the chirality of the experimental set-up is analysed within the density matrix formalism. For two-electron emission we considered two distinct cases. In the first case, we assumed a randomly oriented initial state. The chirality is then imparted to the system via a circularly polarised photon that's absorbed by the two electrons. We showed using a formal tensorial analysis that the continuum spectrum of the electron pair depends in a characteristic way on the helicity of the absorbed photon. The actual magnitude of the chiral effects has been estimated from simple analytical models and more elaborate numerical methods were briefly presented for quantitative predictions. The findings were analysed and interpreted in light of recent

experiments. Furthermore, we envisaged the chiral effects in the photoelectron Auger-electron coincidence spectrum. The Auger hole is created by ionising a randomly oriented target by a circular polarised photon. Thus, the chirality effects are due to a transfer of the photon's helicity to the two escaping electrons. Much of the work discussed here is focused on two active electron systems. It is still unclear in which way the chirality of the photon will be shared in a system with more than two interacting particles, i.e. in one-photon triple ionisation or in excitation double ionisation. A further topic for future research is the behaviour of chiral multi-electron emission from molecular targets. Here, the role of the molecular bond as an additional axis in space is still to be unravelled. Some work in this direction has just been started [53].

In the last section we studied the case in which an atomic target is oriented by optical pumping with circular polarised light. The oriented atomic target is then ionised by low-energy electrons. Here the chirality effect is caused by the initial orientation of the electronic state. We formulated and analysed the theoretical concepts for the transition of the screw sense of the bound valence electron motion to the continuum electron pair. Numerical methods for the calculations of the cross-section for the electron-impact ionisation of oriented atoms are presented and their results are contrasted against recent experimental data.

Current theoretical and experimental research are focused on the role of the electron spin projections [109,108] and on the electron emission from naturally oriented targets, such as ferromagnetic films or molecules oriented on surfaces. For isotropic targets it has been demonstrated [90] that the electron-impact ionisation can be employed as a spectroscopic tool to visualise the electron momentum density in electronic systems. Measuring the chiral effect in the electron-impact ionisation spectrum renders possible an insight into the sense of circulation of the initially bound electron.

Acknowledgements

We are grateful to A. Heutz, P. Selles, V. Schmidt, J.S. Briggs, I. Bray, H. Schmidt-Böcking, V. Mergel, R. Dörner, L. Avaldi, U. Becker, J. Viefhaus and N. Fominykh for many stimulating discussions on the one-photon double ionisation and Prof. A. Yagishita for the permission to use the data of his group.

We are indebted to E. Weigold, J. Lower, A. Dorn, A. Elliott, M. Fehr and S. Mazevet for many encouraging and stimulating discussions and consultations on the ionisation of oriented targets.

Appendix A

In this section we derive analytical relations for the circular dichroism and for the cross-sections of the one-photon double ionisation using simple dynamical models for the motion of the two electrons in the field of the ion.

A.1. The analytical form of the circular dichroism

In this appendix we derive analytical expressions for the double-ionisation cross-section upon the absorption of one circularly polarised photon. Closed analytical relation for the circular

dichroism CD are obtained. For the analysis we employ the wave functions (3.39) and (3.40) for the initial and the final state, respectively. The integrals involved in calculating the cross-sections can be reduced to Fourier transforms of the type

$$\mathscr{I} = \int \mathrm{d}^3 r\, \hat{\varepsilon}\cdot\boldsymbol{r} \exp(-\beta r) \exp(\mathrm{i}\boldsymbol{p}\cdot\boldsymbol{r})\, {}_1F_1(-\mathrm{i}\alpha, 1, \mathrm{i}[kr + \boldsymbol{k}\cdot\boldsymbol{r}]) \tag{A.1}$$

$$= \mathrm{i}\frac{\partial^2}{\partial\beta_d \partial\lambda} \int \mathrm{d}^3 r \frac{\exp(-\beta_d r)}{r} \exp(\mathrm{i}\boldsymbol{p}\cdot\boldsymbol{r} + \mathrm{i}\lambda\hat{\varepsilon}\cdot\boldsymbol{r})\, {}_1F_1(-\mathrm{i}\alpha, 1, \mathrm{i}[kr + \boldsymbol{k}\cdot\boldsymbol{r}])\Big|_{\lambda=0,\beta_d=\beta}$$

$$= \mathrm{i}\frac{\partial^2}{\partial\beta_d \partial\lambda} \frac{4\pi}{\beta_d^2 + P^2} \left[\frac{(\boldsymbol{P}+\boldsymbol{k})^2 - (k + \mathrm{i}\beta_d)^2}{\beta_d^2 + P^2}\right]^{\mathrm{i}\alpha}\Bigg|_{\lambda=0,\beta_d=\beta}, \tag{A.2}$$

where $\boldsymbol{P} := \boldsymbol{p} + \lambda\hat{\varepsilon}$. Employing the wave function (3.39) and (3.40) for the initial and the final state and making use of Eq. (A.2), the cross-section [Eq. (3.1)] can be written in the form

$$\mathrm{W} = C_a |J_b I_a + J_a I_b|^2 , \tag{A.3}$$

where

$$C_a = 128 k_a k_b \omega \alpha_c |N_s N_a N_b N_{ab}|^2 . \tag{A.4}$$

After some algebraic manipulation, the functions I_j, J_j, $j = a, b$ in Eq. (A.3) can be expressed as

$$I_j = -\mathrm{i}(1 + \mathrm{i}\beta_j)\boldsymbol{B}_j \cdot \hat{\varepsilon} \tag{A.5}$$

and

$$J_j = f_j \left[\frac{Z_s + \beta_j k_j}{(k_j^2 + Z_s^2)^2}\right] . \tag{A.6}$$

In Eq. (A.6) the real scalars f_j are given by

$$f_j := \exp\left[2\beta_j \arctan\left(\frac{k_j}{Z_s}\right)\right] , \tag{A.7}$$

whereas in Eq. (A.5) the real vectors $\boldsymbol{B}_j$ read

$$\boldsymbol{B}_j = 2 f_j \left[\frac{2Z_s - Z}{(k_j^2 + Z_s^2)^3}\right] \boldsymbol{k}_j . \tag{A.8}$$

We further define the real vectors $\boldsymbol{A}_a = \boldsymbol{B}_a J_b$, $\boldsymbol{A}_b = \boldsymbol{B}_b J_a$ and the un-normalised dichroism as $\Delta = \mathrm{W}(\sigma^+) - \mathrm{W}(\sigma^-)$. From Eq. (A.3) an expression derives for Δ:

$$\Delta = C_a[(1 + \mathrm{i}\beta_a)\boldsymbol{A}_a \cdot \hat{\varepsilon} + (1 + \mathrm{i}\beta_b)\boldsymbol{A}_b \cdot \hat{\varepsilon}]\,[(1 - \mathrm{i}\beta_a)\boldsymbol{A}_a \cdot \hat{\varepsilon}^* + (1 - \mathrm{i}\beta_b)\boldsymbol{A}_b \cdot \hat{\varepsilon}^*]$$
$$- C_a[(1 + \mathrm{i}\beta_a)\boldsymbol{A}_a \cdot \hat{\varepsilon}^* + (1 + \mathrm{i}\beta_b)\boldsymbol{A}_b \cdot \hat{\varepsilon}^*]\,[(1 - \mathrm{i}\beta_a)\boldsymbol{A}_a \cdot \hat{\varepsilon} + (1 - \mathrm{i}\beta_b)\boldsymbol{A}_b \cdot \hat{\varepsilon}] . \tag{A.9}$$

The latter equation can be simplified to

$$\Delta = -2\mathrm{i}C_a(\beta_b - \beta_a)\,[(\boldsymbol{A}_a \times \hat{\varepsilon})(\boldsymbol{A}_b \times \hat{\varepsilon}^*) - (\boldsymbol{A}_a \times \hat{\varepsilon}^*)(\boldsymbol{A}_b \times \hat{\varepsilon})] . \tag{A.10}$$

Making use of the re-coupling formula, given by Eq. (3.6), we can write Eq. (A.10) in the form

$$\Delta = -ZF(k_a - k_b)(\hat{\boldsymbol{k}}_a \times \hat{\boldsymbol{k}}_b)\cdot\hat{\boldsymbol{k}} . \tag{A.11}$$

The function F is then given by

$$F = 2C_a(Z_s - Z)^2(2Z_s - Z)^2(2f_a f_b)^2(k_a^2 + Z_s^2)^{-5}(k_b^2 + Z_s^2)^{-5} . \tag{A.12}$$

For the present study it is important to note that F [Eq. (A.12)] is angular independent and positive definite for all k_a, k_b.

A.2. Analytical expressions for the one-photon double-ionisation cross-section

Eq. (A.11) is the expression for the un-normalised dichroism. To emphasise the independence of the Δ and $W(\sigma^{\pm})$ we define a normalised circular dichroism, CD, as

$$\mathrm{CD} = \frac{\Delta}{\Sigma} , \tag{A.13}$$

where

$$\Sigma := \mathrm{W}(\sigma^+) + \mathrm{W}(\sigma^-) . \tag{A.14}$$

From Eq. (A.3) and after lengthy, but straightforward algebraic manipulation we deduce

$$\begin{aligned}\Sigma = 2C_a\{&(1 + \beta_a^2)|\boldsymbol{A}_a \cdot \hat{\varepsilon}|^2 + (1 + \beta_b^2)|\boldsymbol{A}_b \cdot \hat{\varepsilon}|^2 \\ &+ (1 + \beta_a\beta_b)\,[(\boldsymbol{A}_a \cdot \hat{\varepsilon})(\boldsymbol{A}_b \cdot \hat{\varepsilon}^*) + (\boldsymbol{A}_b \cdot \hat{\varepsilon})(\boldsymbol{A}_a \cdot \hat{\varepsilon}^*)]\} .\end{aligned} \tag{A.15}$$

Making use of Eqs. (A.5), (A.6) and (A.8), Eq. (A.15) can be reduced to

$$\begin{aligned}\Sigma = 2C_a(2f_a f_b)^2\frac{(Z_s - Z)^2(2Z_s - Z)^2}{(k_a^2 + Z_s^2)^4(k_b^2 + Z_s^2)^4}\Bigg\{&\frac{k_a^2 + Z^2}{(k_a^2 + Z_s^2)^2}|\hat{\boldsymbol{k}}_a \cdot \hat{\varepsilon}|^2 + \frac{k_b^2 + Z^2}{(k_b^2 + Z_s^2)^2}|\hat{\boldsymbol{k}}_b \cdot \hat{\varepsilon}|^2 \\ &+ 2\frac{k_a k_b + Z^2}{(k_a^2 + Z_s^2)(k_b^2 + Z_s^2)}\Re[(\hat{\boldsymbol{k}}_a \cdot \hat{\varepsilon})(\hat{\boldsymbol{k}}_b \cdot \hat{\varepsilon}^*)]\Bigg\} .\end{aligned} \tag{A.16}$$

Now combining Eqs. (A.16) and (A.11) we end up with the final result for the CD

$$\mathrm{CD} := -\frac{Z}{\mathscr{F}}(k_a - k_b)(\hat{\boldsymbol{k}}_a \times \hat{\boldsymbol{k}}_b) \cdot \hat{\boldsymbol{k}} , \tag{A.17}$$

where $\mathscr{F}$ is positive definite in the six-dimensional $\boldsymbol{k}_a \otimes \boldsymbol{k}_b$ space and has the form

$$\begin{aligned}\mathscr{F} = &\frac{k_b^2 + Z_s^2}{k_a^2 + Z_s^2}(k_a^2 + Z^2)|\hat{\boldsymbol{k}}_a \cdot \hat{\varepsilon}|^2 + \frac{k_a^2 + Z_s^2}{k_b^2 + Z_s^2}(k_b^2 + Z^2)|\hat{\boldsymbol{k}}_b \cdot \hat{\varepsilon}|^2 \\ &+ 2(k_a k_b + Z^2)\Re[(\hat{\boldsymbol{k}}_a \cdot \hat{\varepsilon})(\hat{\boldsymbol{k}}_b \cdot \hat{\varepsilon}^*)] .\end{aligned} \tag{A.18}$$

References

[1] R.T. Morrison, R.N. Boyd, Organic Chemistry, Allyn and Bacon Inc., Boston, USA, 1968.
[2] I. Hodgkinson, Q.H. Wu, B. Knight, A. Lakhtakia, K. Robbie, Appl. Opt. 39 (4) (2000) 642–649.
[3] Y.R. Shen, The Principles of Nonlinear Optics, Wiley, New York, 1984.

[4] M.V. Hobden, Nature 216 (1967) 678.
[5] R. Williams, Phys. Rev. Lett. 21 (1968) 342.
[6] T. Verbiest, M. Kauranen, A. Persoons, Phys. Rev. Lett. 82 (18) (1999) 3601–3604.
[7] C. Westphal, J. Bansmann, M. Getzlaff, G. Schönhense, Phys. Rev. Lett. 63 (1989) 151.
[8] F. Heiser, O. Geßner, U. Hergenhan, J. Viefhaus, K. Wieliczek, N. Saito, U. Becker, J. Electron Spectrsc. Related Phenom. 79 (1996) 415.
[9] V.V. Kuznetsov, N.A. Cherepkov, G.H. Fecher, G. Schönhense, J. Chem. Phys. 110 (1999) 9997–10000.
[10] V.V. Kuznetsov, N.A. Cherepkov, G. Raseev, J. Phys.: Condens. Matter 8 (1996) 10327–10345.
[11] N.A. Cherepkov, G. Raseev, J. Chem. Phys. 103 (1995) 8238–8246.
[12] J. Bansmann, C. Ostertag, M. Getzlaff, G. Schönhense, N.A. Cherepkov, V.V. Kuznetsov, A.A. Pavlychev, Z. Phys. D 33 (1995) 257–264.
[13] N.A. Cherepkov, G. Schönhense, Europhys. Lett. 24 (1993) 79–85.
[14] C. Westphal, J. Bansmann, M. Getzlaff, G. Schönhense, N.A. Cherepkov, M. Braunstein, V. McKoy, R.L. Dubs, Surf. Sci. 253 (1991) 205–219.
[15] C.N. Yang, Phys. Rev. 74 (1948) 764.
[16] V.L. Jacobs, J. Phys. B 5 (1972) 2257.
[17] N.A. Cherepkov, Phys. Lett. A 40 (1972) 119–121.
[18] N.A. Cherepkov, Adv. At. Mol. Phys. 19 (1983) 395–447.
[19] C.M. Lee, Phys. Rev. A 10 (1974) 1598–1604.
[20] U. Heinzmann, 13 (1980) 4367–4381.
[21] Ch. Heckenkamp, F. Schäfer, G. Schönhense, U. Heinzmann, Z. Phys. D 2 (1986) 257–274.
[22] G. Baum, M.S. Lubell, W. Raith, Phys. Rev. Lett. 25 (1970) 267–270.
[23] H. Klar, H. Kleinpoppen, J. Phys. B. (1982) 15933–15950.
[24] V.V. Balashov, N.A. Grum-Grzhimailo, V. Zhadamba, Opt. Spectrosc. 65 (1988) 315–319.
[25] S. Baier, N.A. Grum-Grzhimailo, N.M. Kabachnik, J. Phys. B 27 (1994) 3363–3388.
[26] R.L. Dubs, S.N. Dixit, V. McKoy, Phys. Rev. B 32 (1985) 8389–8391.
[27] N.A. Cherepkov, V.V. Kuznetsov, V.A. Verbitskii, J. Phys. B 28 (1995) 1221–1239.
[28] L.E. Cuéllar, C.S. Feigerle, H.S. Carman Jr., R.N. Compton, Phys. Rev. A 43 (1991) 6437–6440.
[29] C. Kerling, N. Böwering, U. Heinzmann, J. Phys. B 23 (1990) L629–L635.
[30] M. Pahler, C. Lorenz, E.V. Raven, J. Rüder, B. Sonntag, S. Baier, B.R. Müller, M. Schulze, H. Staiger, P. Zimmermann, N.M. Kabachnik, Phys. Rev. Lett. 68 (1992) 2285–2288.
[31] S. Baier, M. Schulze, H. Staiger, P. Zimmermann, C. Lorenz, M. Pahler, J. Rüder, B. Sonntag, J.T. Costello, L. Kieman, J. Phys. B 24 (1994) 1341–1349.
[32] L. Baumgarten, C.M. Schneider, H. Petersen, F. Schäfer, J. Kirschner, Phys. Rev. Lett. 65 (1990) 492–495.
[33] D. Venus, W. Kuch, T.-M. Lin, C.M. Schneider, H. Ebert, J. Kirschner, Phys. Rev. B 55 (1997-II) 2594.
[34] J. Henk, A.M.N. Niklasson, B. Johansson, Phys. Rev. B 59 (1999) 13 986.
[35] J. Braun, Rep. Prog. Phys. 59 (1996) 1267.
[36] J. Berakdar, H. Klar, Phys. Rev Lett. 69 (1992) 1175.
[37] J. Berakdar, H. Klar, A. Huetz, P. Selles, J. Phys. B 26 (1993) 1463.
[38] N.M. Kabachnik, V. Schmidt, J. Phys. B 28 (1995) 233.
[39] N. Chandra, S. Sen, Phys. Rev. A 52 (1995) 2820–2828.
[40] N.L. Manakov, S.I. Marmo, A.V. Meremianin, J. Phys. B 29 (1996) 2711.
[41] A.W. Malcherek, J.S. Briggs, J. Phys. B 30 (1997) 4419.
[42] J. Viefhaus, L. Avaldi, G. Snell, M. Wieddenhöft, R. Hentges, A. Rüdel, F. Schäfers, D. Menke, U. Heinzmann, A. Engelns, J. Berakdar, H. Klar, U. Becker, Phys. Rev. Lett. 77 (1996) 3975.
[43] V. Mergel, M. Achler, R. Dörner, Kh. Khayyat, T. Kambara, Y. Awaya, V. Zoran, B. Nyström, L. Spielberger, J.H. McGuire, J. Feagin, J. Berakdar, Y. Azuma, H. Schmidt-Böcking, Phys. Rev. Lett. 80 (1998) 5301.
[44] J. Berakdar, J. Phys. B 31 (1998) 3167.
[45] J. Berakdar, J. Phys. B 32 (1999) L27.
[46] A.S. Kheifets, I. Bray, J. Phys. B 31 (1998) L447.
[47] A.S. Kheifets, I. Bray, Phys. Rev. Lett. 81 (1998) 4588.

[48] L. Malegat, P. Selles, A. Huetz, J. Phys. B 30 (1997) 251.
[49] L. Malegat, P. Selles, P. Lablanquie, J. Mazeau, A. Huetz, A J. Phys. B 30 (1997) 263.
[50] K. Soejima, A. Danjo, K. Okuno, A. Yagishita, Phys. Rev. Lett. 83 (1999) 1546.
[51] K. Soejima, M. Shimbo, A. Danjo, K. Okuno, E. Shigemasa, A. Yagishita, J. Phys. B 29 (1996) L367.
[52] T. Aberg, S. Heinäsmäki, Appl. Phys. A 65 (1997) 131.
[53] T.J. Reddish, J.M. Feagin, J. Phys. B 32 (1999) 2473.
[54] J.S. Briggs, V. Schmidt, J. Phys. B 33 (2000) R1.
[55] Z. Roller-Lutz, Y. Wang, H.O. Lutz, T. Bastug, T. Mukoyama, B. Fricke, Phys. Lett. A 262 (1999) 66–71.
[56] S. Bradenbrink, H. Reihl, T. Wormann, Z. Roller-Lutz, H.O. Lutz, J. Phys. B 27 (1994) L391–L394.
[57] Z. Roller-Lutz, K. Finck, Y. Wang, H.O. Lutz, Phys. Lett. A 169 (1992) 173–176.
[58] A. Dorn, A. Elliot, J. Lower, E. Weigold, J. Berakdar, A. Engelns, H. Klar, Phys. Rev. Lett. 80 (1998) 257.
[59] J. Berakdar, A. Dorn, A. Elliot, J. Lower, E. Weigold, J. Electron Spectrosc. Related Phenom. 88–91 (1998) 50–64.
[60] K. Blum, Density Matrix Theory and Applications, Plenum, New York, 1981.
[61] C. Dal Cappello, H. Le Rouzo, Phys. Rev. A 43 (1991) 1395.
[62] F. Maulbetsch, J.S. Briggs, Phys. Rev. Lett. 68 (1992) 2004.
[63] C. Caroli, D. Lederer-Rozenblatt, B. Roulet, D. Saint-James, Phys. Rev. B 8 (1973) 4552.
[64] N. Fominykh, J. Henk, J. Berakdar, P. Bruno, H. Gollisch, R. Feder, Solid State Commun. 113 (2000) 665–669.
[65] J. Berakdar, Phys. Rev. B 58 (1998) 9808.
[66] J. Berakdar, Appl. Phys. A 69 (1999) 497–501.
[67] R. Herrmann, S. Samarin, H. Schwabe, J. Kirschner, Phys. Rev. Lett. 81 (1998) 2148.
[68] U. Fano, J.H. Macek, Rev. Mod. Phys. 45 (1973) 553.
[69] D.M. Brink, G.R. Satchler, Angular Momentum, 2nd Edition, Clarendon Press, Oxford, 1968.
[70] D.A Varshalovich, A.N. Moskalev, V.K. Khersonskii, Quantum Theory of Angular Momentum, World Scientific, Singapore, 1988.
[71] G. Wannier, Phys. Rev. 90 (1953) 817.
[72] R. Peterkop, J. Phys. B 4 (1971) 513.
[73] A.R.P. Rau, Phys. Rev. A 4 (1971) 207; Phys. Rep. 110 (1984) 369.
[74] A. Huetz, P. Selles, D. Waymel, J. Mazeau, J. Phys. B 24 (1991) 1917.
[75] M. Abramowitz, I.A. Stegun (Eds.), Pocketbook of Mathematical Functions, Verlag Harri Deutsch, Frankfurt a.M., 1984.
[76] J. Berakdar, Phys. Rev. A 53 (1996) 2314.
[77] G. Garibotti, J.E. Miraglia, Phys. Rev. A 21 (1980) 572.
[78] M. Brauner, J.S. Briggs, H. Klar, J. Phys. B 22 (1989) 2265.
[79] J.S. Briggs, Phys. Rev. A 41 (1990) 539.
[80] F. Maulbetsch, J.S. Briggs, J. Phys. B 28 (1995) 551.
[81] H.A. Bethe, E.E. Salpeter, Quantum Mechanics of One- and Two-Electron Atoms, Springer, Berlin, 1957.
[82] H. Kossmann, V. Schmidtand, T. Andersen, Phys. Rev. Lett. 60 (1988) 1226.
[83] H. Bräuning et al., J. Phys. B 31 (1998) 5149.
[84] A. Hylleraas, Z. Phys. D 54 (1929) 347.
[85] S. Bhattacharyya, A. Bhattacharyya, B. Talukdar, N.C. Deb, J. Phys. B 29 (1996) L147.
[86] I. Bray, Phys. Rev. Lett. 78 (1997) 4721.
[87] S.J. Schaphorst, B. Krässig, O. Schwarzkopf, N. Scherer, V. Schmidt, P. Lablanquie, L. Andric, J. Mazeau, A. Huetz, J. Electron Spectrosc. Related Phenom. 76 (1995) 229.
[88] A.S. Kheifets, I. Bray, K. Soejima, A. Danjo, K. Okuno, A. Yagishita, J. Phys. B 32 (1999) L501.
[89] H. Klar, J. Phys. B 13 (1980) 3117.
[90] I.E. McCarthy, E. Weigold, Rep. Prog. Phys. 54 (1991) 789.
[91] K. Bartschat, Phys. Rep. 180 (1988) 1.
[92] J. Kessler, Polarised Electrons, 2nd Edition, Springer, Berlin, 1985.
[93] S. Mazevet, I.E. McCarthy, E. Weigold, Phys. Rev. A 57 (1998) 1881.
[94] I. Percival, M.J. Seaton, Philos. Trans. Roy. Soc. A 251 (1958) 113.
[95] A. Fisher, I.V. Hertel, Z. Phys. A 304 (1981) 103.

[96] M. Inokuti, Rev. Mod. Phys. 43 (1971) 297.
[97] I.E. McCarthy, E. Weigold, Electron–Atom Collisions, Cambridge University Press, Cambridge, 1995.
[98] I.E. McCarthy, Aust. J. Phys. 48 (1995) 1.
[99] J. Berakdar, A. Engelns, H. Klar, J. Phys. B 29 (1996) 1109.
[100] J. Berakdar, Phys. Rev. A 56 (1997) 370.
[101] J. Berakdar, J.S. Briggs, I. Bray, D.V. Fursa, J. Phys. B 32 (1999) 895.
[102] A. Elliot, J. Lower, E. Weigold, S. Mazevet, J. Berakdar, Phys. Rev. A 62 (2000) 012706.
[103] J. Berakdar, S. Mazevet, J. Phys. B 32 (1999) 9365.
[104] J.C. Joachain, The Quantum Collision Theory, North-Holland Publishing Company, Amsterdam, 1983.
[105] J.B. Furness, I.E. McCarthy, J. Phys. B 6 (1973) 2280.
[106] J. Berakdar, J.S. Briggs, Phys. Rev. Lett. 72 (1994) 3799.
[107] J. Berakdar, Aust. J. Phys. 49 (1996) 1095.
[108] P. Golecki, H. Klar, J. Phys. B 32 (1999) 1647.
[109] J. Lower, E. Weigold, S. Mazevet, J. Berakdar, Phys. Rev. Lett., submitted for publication.